Monthly Notices
of the
ROYAL ASTRONOMICAL SOCIETY

MNRAS **449,** 4476–4493 (2015) doi:10.1093/mnras/stv559

Co-evolution of black hole growth and star formation from a cross-correlation analysis between quasars and the cosmic infrared background

Lingyu Wang,[1⋆] Marco Viero,[2] Nicholas P. Ross,[3] Viktoria Asboth,[4] Matthieu Béthermin,[5] Jamie Bock,[2,6] Dave Clements,[7] Alex Conley,[8] Asantha Cooray,[9] Duncan Farrah,[10] Amir Hajian,[11] Jiaxin Han,[1] Guilaine Lagache,[12] Gaelen Marsden,[4] Adam Myers,[13] Peder Norberg,[1] Seb Oliver,[14] Mat Page,[15] Myrto Symeonidis,[14] Bernhard Schulz,[6,16] Wenting Wang[1] and Mike Zemcov[2,6]

[1]*Institute for Computational Cosmology, Department of Physics, Durham University, Durham DH1 3LE, UK*
[2]*California Institute of Technology, 1200 E. California Blvd., Pasadena, CA 91125, USA*
[3]*Department of Physics, Drexel University, 3141 Chestnut Street, Philadelphia, PA 19104, USA*
[4]*Department of Physics and Astronomy, University of British Columbia, 6224 Agricultural Road, Vancouver, BC V6T 1Z1, Canada*
[5]*European Southern Observatory, Karl-Schwarzschild-Str. 2, D-85748 Garching, Germany*
[6]*Jet Propulsion Laboratory, 4800 Oak Grove Drive, Pasadena, CA 91109, USA*
[7]*Astrophysics Group, Blackett Laboratory, Imperial College of Science Technology and Medicine, London SW7 2BZ, UK*
[8]*Center for Astrophysics and Space Astronomy 389-UCB, University of Colorado, Boulder, CO 80309, USA*
[9]*Center for Cosmology, Department of Physics and Astronomy, University of California, Irvine, CA 92697, USA*
[10]*Department of Physics, Virginia Tech, Blacksburg, VA 24061, USA*
[11]*Canadian Institute for Theoretical Astrophysics, University of Toronto, Toronto, ON M5S 3H8, Canada*
[12]*Institut d'Astrophysique Spatiale (IAS), Bâtiment 121, F- 91405 Orsay (France); Université Paris-Sud 11 and CNRS (UMR 8617)*
[13]*Department of Physics and Astronomy, University of Wyoming, Laramie, WY 82071, USA*
[14]*Astronomy Centre, Department of Physics & Astronomy, University of Sussex, Brighton BN1 9QH, UK*
[15]*Mullard Space Science Laboratory, University College London, Holmbury St Mary, Dorking, Surrey RH5 6NT, UK*
[16]*Infrared Processing and Analysis Center, MS 100-22, California Institute of Technology, JPL, Pasadena, CA 91125, USA*

Accepted 2015 March 11. Received 2015 March 9; in original form 2014 June 20

ABSTRACT

We present the first cross-correlation measurement between Sloan Digital Sky Survey type 1 quasars and the cosmic infrared background (CIB) measured by *Herschel*. The quasars cover the redshift range $0.15 < z < 3.5$ where most of the CIB originates. We detect the sub-millimetre emission of the quasars, which dominates on small scales, and correlated emission from dusty star-forming galaxies (DSFGs) dominant on larger scales. The mean flux of the Data Release 7 (DR7) quasars (median redshift $\langle z \rangle = 1.4$) is 11.1, 7.1 and 3.6 mJy at 250, 350 and 500 μm, respectively, while the mean flux of the DR9 quasars ($\langle z \rangle = 2.5$) is 5.7, 5.0 and 1.8 mJy at 250, 350 and 500 μm, respectively. Assuming a modified blackbody spectral energy distribution with a power law in the mid-infrared, we infer that the mean infrared luminosity of the DR7 and DR9 quasars is $10^{12.4}$ and $10^{12.8}$ $L_{\odot}$, respectively. The correlated emission arises from DSFGs in the same halo as the quasar (the one-halo term) and DSFGs in separate haloes correlated with the quasar-hosting halo (the two-halo term). Using a simple halo model, we find that most quasars are hosted by central galaxies. The host halo mass scale of the DR7 central and satellite quasars is $10^{12.4\pm0.9}$ and $10^{13.6\pm0.4}$ $M_{\odot}$, respectively. The host halo mass scale of the DR9 central and satellite quasars is $10^{12.3\pm0.6}$ and $10^{12.8\pm0.4}$ $M_{\odot}$, respectively. Thus, the halo environment of the central quasars is similar to that of the most actively star-forming galaxies, which supports the view that dusty starburst and quasar activity are evolutionarily linked.

Key words: galaxies: evolution – galaxies: haloes – galaxies: high-redshift – quasars: general – submillimetre: galaxies.

⋆E-mail: lingyu.wang25@gmail.com

© 2015 The Authors
Published by Oxford University Press on behalf of the Royal Astronomical Society

Downloaded from http://mnras.oxfordjournals.org/ at University of Durham on February 11, 2016

1 INTRODUCTION

Quasars, powered by accretion of material on to the central supermassive black holes (SMBHs) in active galaxies, are among the most luminous objects in the Universe. In the current paradigm of galaxy formation and evolution, quasars represent a key phase in the evolutionary history of massive galaxies. Essentially all spheroidal systems are believed to harbour massive black holes (BH). The masses of the central SMBHs are shown to correlate with many properties of their host galaxies, e.g. the stellar velocity dispersion, mass and luminosity of the bulge (e.g. Kormendy & Richstone 1995; Magorrian et al. 1998; Ferrarese & Merritt 2000; Gebhardt et al. 2000; Tremaine et al. 2002; Kormendy, Bender & Cornell 2011). Present-day SMBHs are thought to have gained most of their mass via accretion during an active nuclear phase, e.g. the quasar phase. The implication is that black hole growth and star formation activity are inextricably linked, at least for galaxies which experience 'wet' major mergers and a quasar-like period of rapid black hole growth (see Kormendy & Ho 2013, for a review). A probable scenario is that the galaxy initially forms in a gas-rich rotationally supported system. As the host dark matter halo grows, some mechanisms, such as major merger or disc/bar instability trigger a period of rapid, dust obscured star formation activity (starburst) which produces a stellar bulge. At the same time, the infalling gas fuelling the starburst is feeding the central black hole. After some time the quasar becomes optically visible (unobscured), and soon after that the ongoing star formation is quenched on a short time-scale, perhaps via radiative or mechanical feedback from the central engine (see Fabian 2012, for a review). The cosmic star-formation history is shown to be similar to the evolving luminosity density of quasars (related to the BH accretion history) at most redshifts (e.g. Boyle & Terlevich 1998; Franceschini et al. 1999; Merloni, Rudnick & Di Matteo 2004; Shankar & Mathur 2007; Silverman et al. 2008; Wall, Pope & Scott 2008) , which adds further support to this picture of the galaxy–BH connection.

In this paper, we probe the co-evolution of black hole growth and star formation activity using a cross-correlation analysis between optically selected type 1 quasars over $0.2 < z < 3.5$ and the cosmic infrared background (CIB) in the far-infrared (FIR)/sub-millimetre (sub-mm). The former represents some of the most luminous and massive BHs found to date. The latter is dominated by emission from dusty star-forming galaxies (DSFGs) over a similar redshift range to the quasars (Valiante et al. 2009; Béthermin et al. 2011, 2012; Viero et al. 2013). The large-scale cross-correlation is determined by the effective linear bias (or equivalently, the effective host halo mass) of both sets of tracers of the underlying large-scale structure. The small-scale cross-correlation constrains the halo occupation distributions (HODs) of DSFGs in haloes hosting quasars and the HODs of quasars in haloes hosting DSFGs. In contrast, the auto-correlation function constrains the HODs of each population independently, not the HODs of one population in the presence of the other. Therefore, the cross-correlation function is arguably more suited to studying the co-evolution of the quasars and the star-forming galaxies.[1]

[1] Ideally, one can combine the cross- and auto-correlation functions to constrain the HODs of different galaxy populations. In practice, however, the auto-correlation function is more difficult to measure accurately because it is very sensitive to how well we can understand and reproduce the selection effects of the sample. In contrast, uncorrelated selection effects only affect the uncertainty but do not bias measurement of the cross-correlation signal.

Quasars are very luminous active galactic nuclei (AGN) and hence can be seen out to great distances. They are great tracers of the large-scale structure. To measure their clustering properties reliably, large-volume surveys are required, due to the low spatial density of quasars. The Sloan Digital Sky Survey (SDSS; York et al. 2000) has produced some of the largest quasar samples to date and that is what we use in this paper.

FIR and sub-mm observations are critical for studying star-forming galaxies, as dust absorbs the optical/ultraviolet light and reradiates in the FIR/sub-mm. Dust emission makes up the CIB, which contains half of the extragalactic background radiation (excluding the cosmic microwave background), i.e. the total power originated from stars and AGN throughout the cosmic history (Puget et al. 1996; Fixsen et al. 1998; Lagache, Puget & Gispert 1999). The *Herschel Space Observatory*[2] (Pilbratt et al. 2010) has carried out imaging surveys of unprecedented size and depth in the FIR/sub-mm. It allows us for the first time to probe the bolometric power of DSFGs at high redshift in large volumes.

This paper is organized as follows. In Section 2, we give an overview of the *Herschel*-SPIRE maps and SDSS DR7 and DR9 quasar catalogues used in our analysis. In Section 3, we first describe the estimator used to calculate the cross-correlation. We then investigate the potential contamination of Galactic dust emission using the cross-correlation between quasars and the *IRAS* 100 μm data. Finally, we present the cross-correlation between various quasar samples and the SPIRE (Spectral and Photometric Imaging Receiver) maps at 250, 350 and 500 μm. In Section 4, a halo model is employed to interpret the measured quasar–CIB cross-correlation and constrain the HODs of quasars in haloes that also host star-forming galaxies. Further discussion and conclusions are given in Section 5. We assume an $H_0 = 70$ km s^{-1} Mpc^{-1}, $\Omega_{\rm M} = 0.3$ and $\Omega_\Lambda = 0.7$ cosmology and use the AB magnitude scale throughout the paper.

2 DATA

2.1 *Herschel*-SPIRE maps

We use CIB maps at 250 (the PSW filter), 350 (the PMW filter) and 500 (the PLW filter) μm (1200, 857 and 600 GHz, respectively) from the two *Herschel* surveys in the SDSS Stripe 82 region ($-50^\circ < {\rm RA} < 59^\circ$, $-1.^\circ25 < {\rm Dec} < 1.^\circ25$), i.e. the *Herschel* Stripe 82 Survey (HeRS;[3] Viero et al. 2014) and the HerMES[4] Large-Mode Survey (HeLMS; Oliver et al. 2012). Maps were observed with the SPIRE instrument (Griffin et al. 2010) aboard *Herschel*. HeRS covers 79 deg^2 along the SDSS Stripe 82 to a 5σ depth of 65.0, 64.5 and 74.0 mJy beam^{-1} at 250, 350 and 500 μm, respectively. HeLMS covers 270 deg^2 to a 5σ depth of 71.1, 71.5 and 79.9 mJy beam^{-1} at 250, 350 and 500 μm. The joint HeRS and HeLMS areal coverage between -10° and 37° (RA) covers the full $\sim$150 deg^2 subset of Stripe 82 that has the lowest level of Galactic dust emission (or cirrus) foregrounds (i.e. with $N_{\rm H} \lesssim 2 \times 10^{21}$ cm^{-2}).

[2] *Herschel* is an ESA space observatory with science instruments provided by European-led Principal Investigator consortia and with important participation from NASA.

[3] HeRS maps and point source catalogues can be accessed from http://www.astro.caltech.edu/hers/.

[4] The *Herschel* Multi-tiered Extragalactic Survey (HerMES; http://hermes.sussex.ac.uk) is a guaranteed time key project of the *Herschel Space Observatory*. HerMES maps and point source catalogues are publicly available at http://hedam.lam.fr/HerMES.

Downloaded from http://mnras.oxfordjournals.org/ at University of Durham on February 11, 2016

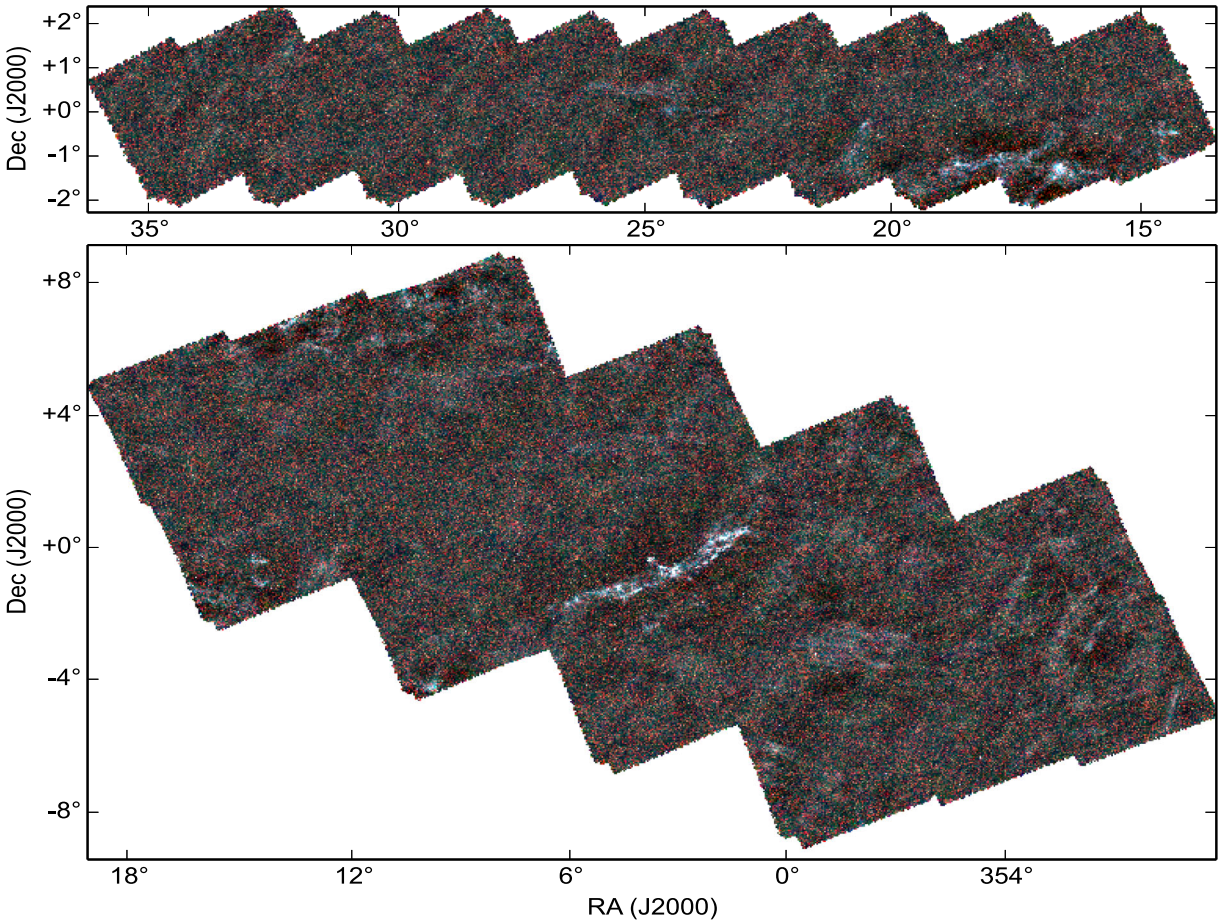

Figure 1. Three-colour SPIRE images of the HeRS (top) and HeLMS (bottom) fields with 250, 350 and 500 μm as blue, green and red, respectively. Foreground clouds of Galactic cirrus can be clearly seen. The area of HeRS and HeLMS is 79 and 270 deg^2, respectively. Jointly, they cover the full 150 deg^2 subset of the SDSS Stripe 82 region ($-50^\circ < \mathrm{RA} < 59^\circ$, $-1\overset{\circ}{.}25 < \mathrm{Dec} < 1\overset{\circ}{.}25$) that has the lowest level of Galactic cirrus.

The SPIRE data, obtained from the *Herschel* Science Archive, were reduced using the standard ESA software and the custom-made software package, SMAP (Levenson et al. 2010; Viero et al. 2014). Maps were made using an updated version of SMAP/SHIM, which is an iterative map-maker designed to optimally separate large-scale noise from signal. For more details, please refer to Viero et al. (2014). The maps have a tangent plane projection with pixel sizes of 6, 8.33 and 12 arcsec at 250, 350 and 500 μm, respectively. In comparison, the full width at half-maximum (FWHM) of the beams is 18.1, 25.2 and 36.6 arcsec at 250, 350 and 500 μm, respectively (Swinyard et al. 2010). The SPIRE maps are converted from their native unit of Jy beam^{-1} to Jy sr^{-1} by dividing them by the effective beam areas which are 0.9942, 1.765 and 3.730 $\times$ 10^{-8} sr at 250, 350 and 500 μm, respectively (SPIRE Observers' Manual[5]). We note that no colour corrections from a flat-spectrum point source calibration are applied, as they were shown in Viero et al. (2013) to be negligible. Fig. 1 shows the three-colour SPIRE images of the HeRS and HeLMS regions. We can clearly see white foreground clouds of Galactic cirrus emission, which have been shown to correlate with H I emission from the Parkes Galactic All-Sky Survey 21-cm data in Viero et al. (2014).

In this paper, we also include SPIRE maps of a subset of the HerMES level 5 and 6 fields,[6] which have significant overlaps with our quasar samples. In particular, the Boötes field (11.3 deg^2) and the Lockman-SWIRE field (15.2 deg^2) overlap with the SDSS DR7 quasar sample. Boötes and *XMM*-LSS (21.6 deg^2) overlap with the SDSS DR9 quasar sample. Fig. 2 shows the SPIRE images of Boötes, Lockman-SWIRE and *XMM*-LSS. Out of these three fields, *XMM*-LSS is the most contaminated by cirrus, but all three fields have significantly less cirrus contamination than HeRS or HeLMS. In addition, the level 5 and 6 fields are significantly deeper. The 5σ noise level in *XMM*-LSS and Boötes is 25.8, 21.2 and 30.8 mJy beam^{-1} at 250, 350 and 500 μm, respectively. Lockman-SWIRE is even deeper and the 5σ noise level is 13.6, 11.2 and 16.2 mJy beam^{-1} at 250, 350 and 500 μm, respectively.

The CIB in the sub-mm is dominated by emission from DSFGs over a wide range of redshift, while other potential sources of signal, e.g. the cosmic microwave background (CMB), Sunyaev-Zel'dovich effect and radio galaxies, are subdominant. One exception is the emission from Galactic dust (cirrus) which cannot be ignored. Therefore, the SPIRE maps can be modelled, to first order,

[5] http://herschel.esac.esa.int/Docs/SPIRE/html/spire_handbook.html

[6] HerMES fields are organized, according to area and depth, into levels 1 through to 7, with level 1 fields being the smallest and deepest, and level 7 being the widest and shallowest. HeLMS is the only level 7 field.

Downloaded from http://mnras.oxfordjournals.org/ at University of Durham on February 11, 2016

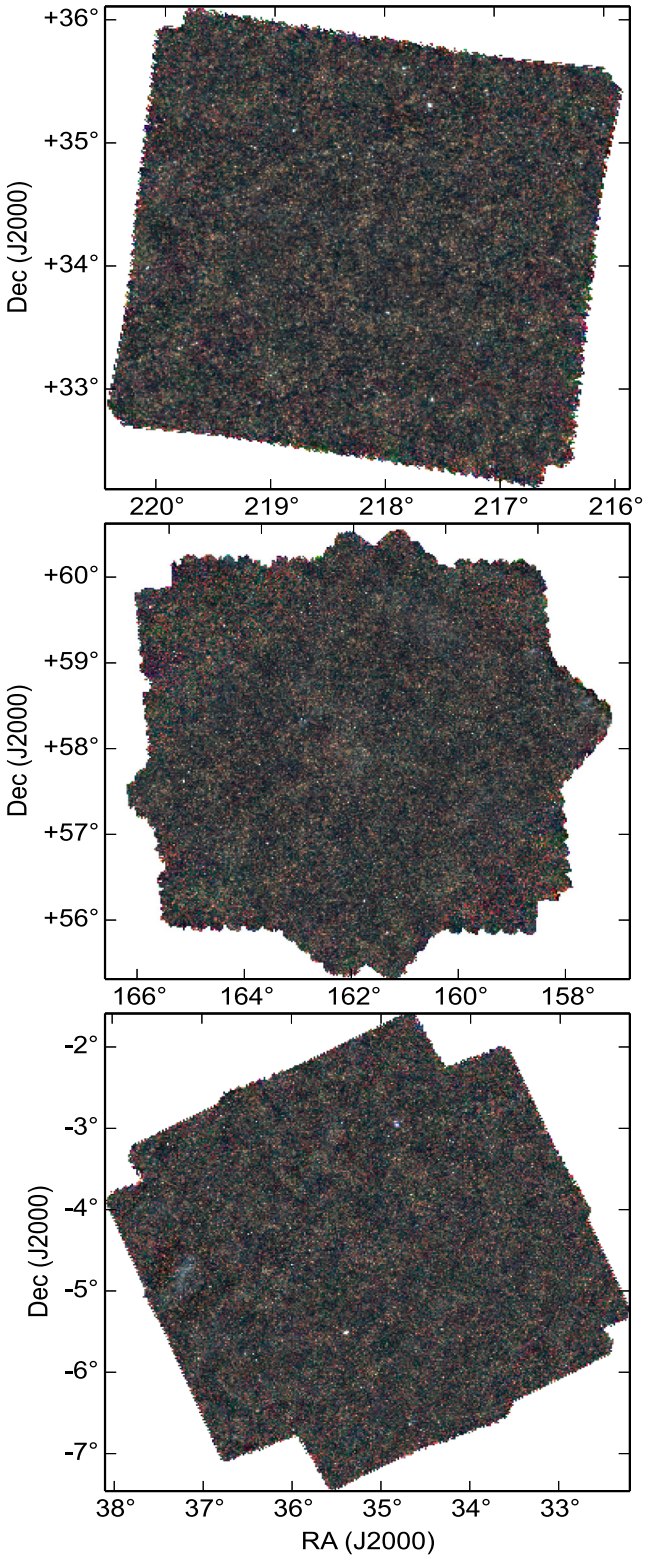

Figure 2. Three-colour SPIRE images of the Boötes (top), Lockman-SWIRE (middle) and *XMM*-LSS field (bottom).

as the sum of three terms: the emission from DSFGs, cirrus and instrument noise,

$$I_{\rm sky} = I_{\rm DSFG} + I_{\rm cirrus} + I_{\rm noise}. \quad (1)$$

We expect that only DSFGs have intrinsic correlation with the quasars. This is because some quasars could be strong IR/sub-mm emitters from dust heated by the accreting BH, as well as star formation in the host galaxy (e.g. Lutz et al. 2008; Clements et al. 2009; Shi et al. 2009; Serjeant et al. 2010; Bonfield et al. 2011; Dai et al. 2012). Additionally, DSFGs are expected to occur as satellite galaxies in haloes where quasars are found.[7] Another effect is that haloes correlated with the quasar-hosting halo are also expected to host DSFGs. Instrument noise and Galactic dust emission should not correlate with quasars and therefore only contribute to the noise in the measured cross-correlation between quasars and the CIB. However, due to the selection of the quasars, there may be (anti)correlation between the observed quasar number density and the intensity of the cirrus emission. There are two effects of Galactic dust on the selection of quasars. The first effect is reddening which means quasars with extreme reddening will not be selected as targets for spectroscopy. The second effect is extinction, which can cause the quasars to drop out of the target list even before they reach the colour selection stage.

To check the potential correlation between quasars and Galactic cirrus emission, we make use of the 100 μm maps from the Improved Reprocessing of the *IRAS* (Neugebauer et al. 1984) Survey (IRIS; Miville-Deschênes & Lagache 2005), a data set which corrects the original plates for calibration, zero level and striping problems. The IRIS 100 μm maps in the HerMES level 5 and 6 fields are discussed in Viero et al. (2013) and the IRIS 100 μm maps in HeRS and HeLMS are discussed in Hajian et al. (in preparation). The 100 μm maps in all of our fields are shown in Appendix A. Here we assume that the dominant signal in the 100 μm maps comes from Galactic cirrus, not DSFGs comprising the CIB. In other words, these 100 μm maps are used as a cirrus tracer in our fields.[8] Visual inspection confirms that extended diffuse cirrus emissions are the dominant structures (long filamentary chains) in the 100 μm maps, especially in HeRS and HeLMS. The mean value of the 100 μm map in HeLMS, HeRS, *XMM*-LSS, Boötes and Lockman-SWIRE is 3.03, 2.84, 2.30, 1.42 and 1.09 MJy sr^{-1}, respectively. Using the DIRBE (Diffuse Infrared Background Experiment) measurement of the CIB at 100 μm, 14.4 ± 6.3 nW m^{-2} sr^{-1} or equivalently 0.48 ± 0.21 MJy sr^{-1} (Dole et al. 2006), we can estimate that the contribution of the CIB to the 100 μm maps in HeLMS, HeRS, *XMM*-LSS, Boötes and Lockman-SWIRE is 16, 17, 21, 34 and 44 per cent, respectively.

2.2 SDSS DR7 and DR9 quasar samples

For our cross-correlation analysis, we use quasars from the SDSS DR7 (Abazajian et al. 2009) and the SDSS-III BOSS DR9 (Ahn et al. 2012) spectroscopic surveys. One complication is that the depth in Stripe 82 differs from the rest of the SDSS area. Stripe 82 is an equatorial region that has been repeatedly imaged up to 80 times (Abazajian et al. 2009) resulting in co-added data that are ∼2 mag deeper than the single epoch SDSS observations. Stripe 82 covers ∼270 deg^2 (-50° < RA <59°, $-1\overset{\circ}{.}25$ < Dec <$1\overset{\circ}{.}25$).

[7] The satellite fraction of quasars (i.e. quasars hosted by satellite galaxies in the halo) is estimated to be at most a few per cent (Kayo & Oguri 2012; Richardson et al. 2012; Shen et al. 2013). Therefore, most quasars are expected to be central galaxies.

[8] Properties of Galactic cirrus (e.g. column density, dust emissivity and temperature) can vary a lot from field to field. In some regions, the IRIS 100 μm data may not be used as a reliable cirrus tracer as a result of significant contamination from the CIB (Pénin et al. 2012).

Downloaded from http://mnras.oxfordjournals.org/ at University of Durham on February 11, 2016

HeRS and HeLMS cover parts of the Stripe 82 region (see Fig. 1 and Section 2.1).

2.2.1 *SDSS DR7 quasars*

The spectroscopic SDSS DR7 quasar catalogue (DR7Q; Schneider et al. 2010; Shen et al. 2011) contains 105 783 spectroscopically confirmed quasars with i-band absolute magnitude $M_i < -22.0$ and $0.065 < z < 5.46$ over 9380 deg^2. It is the culmination of the SDSS I/II quasar surveys. The quasar target selection is described in detail by Richards et al. (2002). Quasar candidates are selected based on their fluxes and colours in SDSS bands. At redshift $z \lesssim 3$, quasar targets are selected based on their location in *ugri*-colour space and at $z \gtrsim 3$, targets are selected from *griz*-colour space. Quasar candidates passing the *ugri*-colour selection are selected to a flux limit of $i = 19.1$, but since high-redshift quasars are rare, objects lying in regions of colour space corresponding to quasars at $z \gtrsim 3$ are targeted to $i = 20.2$ (PSF magnitudes corrected for Galactic extinction based on the dust maps of Schlegel, Finkbeiner & Davis 1998).

2.2.2 *SDSS-III BOSS DR9 quasars*

The Data Release 9 quasar catalogue (DR9Q; Pâris et al. 2012) is the first quasar catalogue from the Baryon Oscillation Spectroscopic Survey (BOSS; Dawson et al. 2013) of the SDSS III (Eisenstein et al. 2011). The catalogue contains 87 822 quasars over 3275 deg^2. The primary science goal for the high-z BOSS quasar survey was to measure the baryon acoustic oscillations in the Lyman α forest (Busca et al. 2013; Slosar et al. 2013; Delubac et al. 2015). As such a priority was set on obtaining a high surface density of $z > 2.1$ quasars in order to maximize the number of Lyman α forest lines of sight observable in the blue. To achieve this high surface density, quasar candidates were selected in a heterogeneous manner, down to a magnitude limit of $g \leq 22.0$ or $r \leq 21.85$ (Ross et al. 2012). Quasars were selected based on their optical fluxes and colours, as well as their near-infrared, ultraviolet fluxes and radio properties. The nominal i-band limit of the DR9 quasar sample is 21.8, which is deeper than the SDSS imaging limit of 21.3. Ross et al. (2012, and references therein) has full details.

However, a uniform selection was performed on a sub-sample of the DR9 quasar targets. This uniform sample was selected by the 'extreme deconvolution' (XD; Bovy, Hogg & Roweis 2009) algorithm which is applied to model the distribution in flux and flux uncertainty of a training set of quasars and stars (XDquasar; Bovy et al. 2011). The DR9Q has a flag 'uniform >0' which represents quasars selected in this uniform manner. The XD method is specially trained and designed to select quasars in the redshift range $2.2 < z < 3.5$ down to the BOSS limiting magnitude

One complication for DR9 quasars is that a set of quasar selection methods, not just the uniform XDquasar method, were used in the Stripe 82 region. However, during BOSS observations, Stripe 82 was observed at a high target density (Palanque-Delabrouille et al. 2011) and the actual completeness of $2.2 < z < 3.5$ quasars is close to 100 per cent, down to the $g \leq 22.0$ or $r \leq 21.85$ limiting magnitude (Palanque-Delabrouille et al. 2013; Ross et al. 2013).

2.2.3 *Quasar selection and their properties*

Outside Stripe 82, we select DR7 quasars with $i < 19.1$ for the cross-correlation study. Boötes and Lockman-SWIRE overlap with the DR7 quasars outside the Stripe 82 area. Since the Stripe 82 imaging is deeper we are able to select DR7 quasars with $i < 19.9$ inside Stripe 82. Both HeRS and HeLMS cover parts of the Stripe 82. Furthermore, we restrict our analysis to DR7 quasars in the redshift range $0.15 < z < 2.5$, with a median redshift of 1.4. The redshift cut is used to avoid the redshift deserts of quasars at $z \sim 2.7$ and $z \sim 3.5$ due to contamination from F and GK stars (Fan 1999; Richards et al. 2002, 2006). To summarize, we select all DR7 quasars at $0.15 < z < 2.5$ with $i < 19.1$ in Boötes and Lockman-SWIRE and $i < 19.9$ in HeRS and HeLMS.

To construct a statistical DR9 quasar sample for clustering studies, we select all DR9 quasars outside Stripe 82 with 'uniform >0' (Pâris et al. 2012; White et al. 2012). To select DR9 quasars inside Stripe 82, we do not use the 'uniform >0' selection as XD is not used as the main selection method for quasars in Stripe 82 (see Section 2.2.2). Instead, we select DR9 quasars in Stripe 82 with $i < 21.0$. In Section 3.2, we test this selection criterion in detail. HeRS and HeLMS overlap with the DR9 quasar sample in the Stripe 82 region. Boötes and *XMM*-LSS field overlap with the DR9 quasar sample outside Stripe 82. Additionally, we limit the DR9 quasar sample to be in the redshift range $2.2 < z < 3.5$. The median redshift of the selected DR9 quasar sample is $z = 2.5$. To summarize, we select all DR9 quasars at $2.2 < z < 3.5$ with 'uniform >0' in Boötes and *XMM*-LSS and $i < 21.0$ in HeRS and HeLMS.

In Fig. 3, we plot the sky distribution of the selected DR7 and DR9 quasars in the region covered by HeRS and HeLMS. Out of consideration for space, the distributions of the quasars in Boötes, Lockman-SWIRE and *XMM*-LSS are not shown. Based on visual inspection and lack of angular completeness masks, we assume a uniform angular completeness of the DR7 quasars. More discussion on this issue is presented in Section 3.1. We use DR9 quasar angular completeness masks from White et al. (2012) to model the completeness variations outside Stripe 82 (Boötes and *XMM*-LSS). We select the DR9 quasars in HeRS and HeLMS to be within the Stripe 82 region ($-1.^\circ25 < \mathrm{Dec} < 1.^\circ25$) and assume the angular completeness is uniform. In Table 1, we list the number of selected DR7 and DR9 quasars found in various *Herschel* fields.

In the left-hand panel in Fig. 4, we plot the normalized redshift distribution of the quasar samples. The dashed lines correspond to the entire DR7 and DR9 quasar samples, while the solid lines correspond to the selected quasar samples used in the cross-correlation analysis. Compared to the expected redshift distribution of the integrated sub-mm emission at 250, 350 and 500 μm from various models (Valiante et al. 2009; Béthermin et al. 2011, 2012; Viero et al. 2013), we can see that the DR7 and DR9 quasars completely cover the redshift range where the bulk of the sub-mm emission is expected to arise. In the right-hand panel in Fig. 4, we plot the i-band absolute magnitude (taken from Shen et al. 2011) versus redshift for the quasar samples. The DR9 quasar sample, apart from being at higher redshift, also extends to fainter objects.

3 THE CROSS-CORRELATION BETWEEN QUASAR AND CIB

3.1 Cross-correlation estimator

The cross-correlation of the two fields of interest, ρ_1 (the quasar number density field) and ρ_2 (the CIB), is

$$\xi = \langle \delta_1 \delta_2 \rangle = \frac{1}{\overline{\rho}_1 \overline{\rho}_2} \langle (\rho_1 - \overline{\rho}_1)(\rho_2 - \overline{\rho}_2) \rangle \,, \quad (2)$$

Downloaded from http://mnras.oxfordjournals.org/ at University of Durham on February 11, 2016

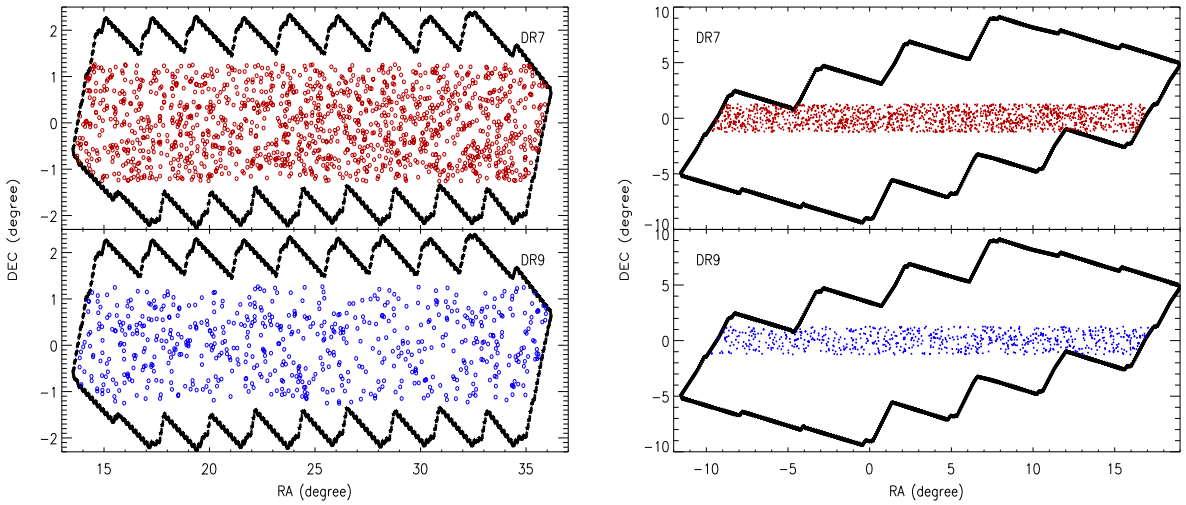

Figure 3. Left: sky distribution of the selected DR7 (top) and DR9 (bottom) quasars in HeRS. The black contours represent the HeRS footprint. Right: sky distribution of the selected DR7 (top) and DR9 (bottom) quasars in HeLMS. The black contours represent the HeLMS footprint. For the DR7 and DR9 quasars, we only use the Stripe 82 region ($-1\overset{\circ}{.}25 <$ Dec $< 1\overset{\circ}{.}25$) in both HeRS and HeLMS.

Table 1. Number of selected DR7 and DR9 quasars in various fields. The second column lists the total area of each field as well as the overlapping area (in brackets) with the quasar samples. Lockman-SWIRE does not overlap with the DR9 quasars and *XMM*-LSS does not overlap with the DR7 quasars.

Field	Area/deg^2	DR7	DR9
HeRS (only the S82 region, $-1\overset{\circ}{.}25 <$ Dec $< 1\overset{\circ}{.}25$)	79 (56)	1411 ($i < 19.9$)	762 ($i < 21.0$)
HeLMS (only the S82 region, $-1\overset{\circ}{.}25 <$ Dec $< 1\overset{\circ}{.}25$)	270 (67)	1675 ($i < 19.9$)	947 ($i < 21.0$)
Boötes	11 (11)	100 ($i < 19.1$)	183 (uniform >0)
Lockman-SWIRE	15 (15)	153 ($i < 19.1$)	–
XMM-LSS	22 (10)	–	117 (uniform >0)

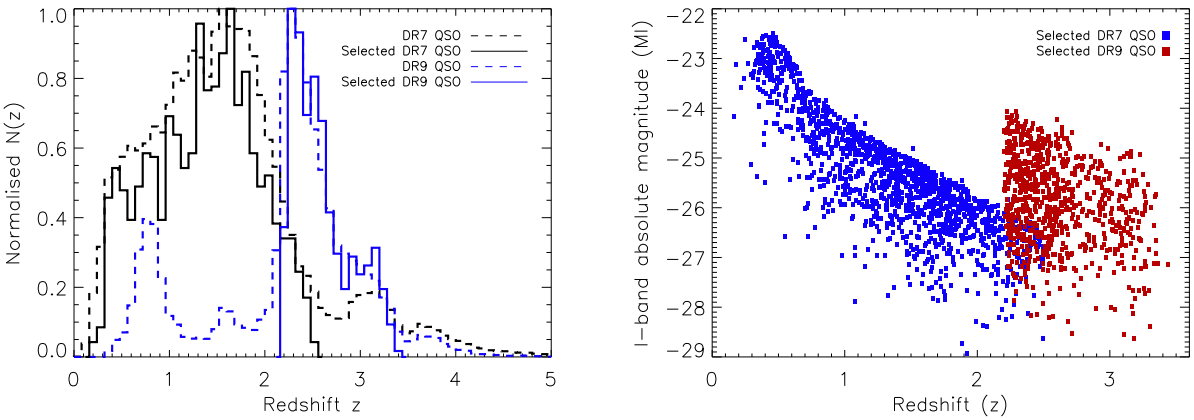

Figure 4. Left: redshift distribution of the DR7 and DR9 quasar sample. The dashed lines correspond the entire DR7 and DR9 samples, while the solid lines correspond to the selected samples used in our analysis. The selected DR7 quasars cover the redshift range $z = [0.15, 2.5]$, with a median redshift $\langle z \rangle = 1.4$, and the selected DR9 quasars cover $z = [2.2, 3.5]$ with $\langle z \rangle = 2.5$. Right: quasar i-band absolute magnitude (taken from Shen et al. 2011) versus redshift. The DR9 quasar sample, apart from being at higher redshift, also includes fainter objects.

where $\overline{\rho}_1$ is the mean number density of quasars and $\overline{\rho}_2$ is the mean value of the CIB. The SPIRE maps, ρ_2', can be used to estimate ρ_2 but they have been mean-subtracted, i.e. $\overline{\rho_2'} = 0$. The two quantities are thus related $\rho_2 = \rho_2' + C$, where C is the unknown DC level of the map. To proceed we assume a value for C and add this to the SPIRE maps[9] and will show that the choice of C only affects the normalization of our results. We define a re-normalized cross-correlation ξ':

$$\xi' = C\xi = \frac{C}{\overline{\rho}_1(\overline{\rho'}_2 + C)}\langle(\rho_1 - \overline{\rho}_1)(\rho_2' + C - (\overline{\rho_2'} + C))\rangle$$
$$= \frac{1}{\overline{\rho}_1}\langle(\rho_1 - \overline{\rho}_1)(\rho_2')\rangle. \quad (3)$$

Equation (3) gives the correlation between the quasar number density field and the SPIRE maps. It is equivalent to the stacked SPIRE

[9] We add a constant C to our mean-subtracted maps so that the minimum value in the map is a positive number.

Downloaded from http://mnras.oxfordjournals.org/ at University of Durham on February 11, 2016

signal at the positions of the quasars minus the mean signal of the map, which is equal to 0 (Marsden et al. 2009). This re-normalized cross-correlation has the same unit as the map.

To estimate the angular cross-correlation function ξ between the quasars and the SPIRE maps, we adapt the Landy & Szalay (1993) auto-correlation estimator,[10]

$$w^{\rm QS}(\theta) = \frac{D_1D_2(\theta) - D_1R_2(\theta) - R_1D_2(\theta) + R_1R_2(\theta)}{R_1R_2(\theta)}. \quad (4)$$

Here, D_1 represents the real quasar sample, D_2 the CIB at a given wavelength, R_1 the simulated quasar sample with the same angular selection as the real sample and R_2 the simulated CIB with the same noise properties as the real maps. $D_1D_2(\theta)$ is the total emission in the CIB map at an angular separation θ from real quasars, $D_1R_2(\theta)$ is the total emission in the simulated CIB map at separation θ from real quasars, $R_1D_2(\theta)$ is the total emission in the CIB map at separation θ from simulated quasars and $R_1R_2(\theta)$ is the total emission of the simulated CIB map at separation θ from simulated quasars. D_1D_2 is normalized by the number of real quasars ($N_{\rm Q}$) times the number of real SPIRE map pixels ($N_{\rm P}$), D_1R_2 is normalized by $N_{\rm Q}$ $\times$ the number of simulated SPIRE map pixels (which is the same as $N_{\rm P}$), R_1D_2 is normalized by the number of simulated quasars ($N_{\rm S}$) $\times$ $N_{\rm P}$, and R_1R_2 is normalized by $N_{\rm S}$ $\times$ $N_{\rm P}$.

The CIB maps are estimated from the mean-subtracted SPIRE maps by adding the same constant number C to represent the mean CIB. As in equation (3), we then estimate a re-normalized cross-correlation signal. So, our actual estimator is[11]

$$\begin{aligned} w'^{\rm QS} &= Cw^{\rm QS}(\theta) \\ &= C\frac{D_1D_2'(\theta) - D_1R_2'(\theta) - R_1D_2'(\theta) + R_1R_2'(\theta)}{R_1(R_2'(\theta) + C)}. \end{aligned} \quad (5)$$

Here, $D_2' = D_2 - C$ is the mean-subtracted SPIRE map, and $R_2' = R_2 - C$ the mean-subtracted simulated SPIRE map. We have checked that the cross-correlation (using equation 5) as well as its error does not depend on the value of C. Although this is a reasonable choice of estimator, we have not investigated whether it is optimal.

The simulated SPIRE maps are made by randomising pixels in the real maps to account for the effects of instrument noise, confusion noise and cirrus. As mentioned before, we assume the angular completeness is uniform for the DR7 quasars. So, we generate uniformly distributed points as the random DR7 quasar sample. Admittedly, the real angular completeness of the DR7 quasars may vary. However, as what we are interested in is the cross-correlation between the quasars and the CIB, the variation in the quasar completeness will not bias our results as long as the completeness is uncorrelated with the noise properties of the CIB maps. For DR9 quasars in Boötes and *XMM*-LSS, we use the angular masks from White et al. (2012) and the MANGLE software (Swanson et al. 2008) to calculate the angular completeness, which is the fraction of quasar targets in a sector for which a spectrum was obtained. For DR9 quasars in the HeRS and HeLMS S82 region, we simply generate uniformly distributed points as the simulated DR9 quasar sample. The number of simulated quasars $N_{\rm S}$ is over 25 times larger than the number of real quasars $N_{\rm Q}$.

[10] The Landy & Szalay estimator is normally used to estimate correlation functions for point source catalogues. Here we use it to calculate the cross-correlation between a point source catalogue and an image.

[11] This is equivalent to stacking, shown in Appendix . We have checked that the cross-correlation calculated using equation (5) is almost identical to the stacking result.

We estimate errors on the two-point angular cross-correlation using 100 bootstrap samples of the quasar sample in each field. The bootstrap samples which have the same size as the real quasar sample are generated by sampling with replacement the real quasar sample (i.e. after a quasar is selected, it is put back in the original catalogue and can be selected again). The dispersion in the signal between the bootstrap quasar samples and the CIB maps is taken as the error on the measured cross-correlation (Norberg et al. 2009).

The method of cross-correlating a catalogue with a map is widely used in cross-correlating CMB maps with large-scale structure traced by galaxies to probe the integrated Sachs–Wolfe effect (e.g. Padmanabhan et al. 2005; Pietrobon, Balbi & Marinucci 2006; Giannantonio et al. 2012). In most studies, the galaxy catalogue (i.e. the quasar catalogue in our case) is used to make a density map with the same pixilation as the map (the CIB maps in our case). Some studies calculate the Fourier-space cross power spectra between the map and the galaxy number density field, while others calculate the real-space angular correlation function between the map and the density field.

3.2 Cross-correlation between quasars and cirrus

There is no intrinsic correlation between quasars and Galactic cirrus. However, the quasar number density could potentially (anti)correlate with the intensity of cirrus emission as quasars are selected based on optical flux and colour. In Fig. 5, we plot the cross-correlation between the quasars and cirrus traced by the IRIS 100 μm maps. The dotted line corresponds to no correlation. The dashed line corresponds to the FWHM of the *IRAS* beam (Miville-Deschênes, Lagache & Puget 2002). Data points below the scale of the beam are strongly correlated. One DR7 quasar in Boötes happens to lie on a bright source in the map, which biases our result (the empty red circles in the top panel in Fig. 5). The filled red circles in the top panel in Fig. 5 show the cross-correlation after excluding the aforementioned quasar. The reduced χ^2 (the degrees of freedom DoF is 8) of the goodness of fit of the dotted line, computed using data above the scale of the beam, is 0.25, 0.24, 0.14 and 0.95 in Boötes, Lockman-SWIRE, HeRS and HeLMS, respectively. For the DR9 quasars, the reduced χ^2 is 0.24 and 0.92 in Boötes and *XMM*-LSS, respectively.

In Fig. 6, we plot the cross-correlation between DR9 quasars with different *i*-band magnitude cuts and IRIS 100 μm maps in the HeRS and HeLMS S82 region. Note that we have not used the 'uniform >0' criterion in selecting DR9 quasars in the Stripe 82 region. The reduced $\chi 2$ in HeRS is 1.29, 0.84 and 0.35 for DR9 quasars with $i < 21.2$, 21.0 and 20.0, respectively. The reduced $\chi 2$ in HeLMS is 0.84, 0.68, and 0.78 for DR9 quasars with $i < 21.2$, 21.0 and 20.0 respectively. We finally select DR9 quasars with $i < 21.0$ in the HeRS and HeLMS S82 region.

In Fig. 7, we plot the combined cross-correlation between the quasars and the 100 μm maps, using inverse variance weighting. The filled circles show the combined signal over all fields and the empty circles show the combined signal using only HeRS and HeLMS. The two are consistent with each other. The cross-correlations between either DR7 or DR9 quasars and the 100 μm maps are consistent with zero. As discussed in Section 2.1, the dominant signal in the 100 μm maps are due to cirrus (especially in HeRS and HeLMS). We conclude that the correlations between the selected quasar samples and Galactic cirrus are consistent with zero.

Downloaded from http://mnras.oxfordjournals.org/ at University of Durham on February 11, 2016

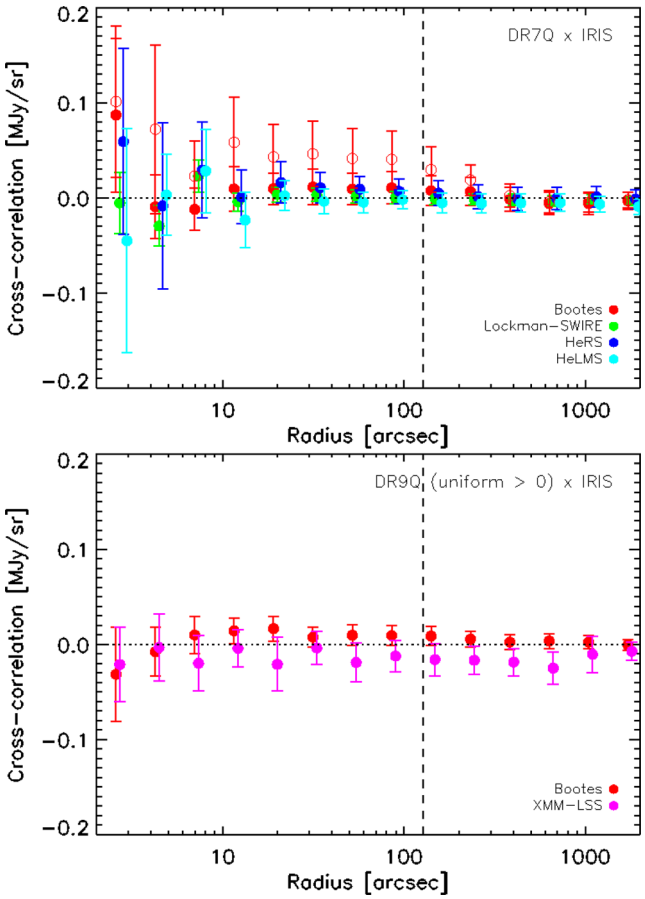

Figure 5. Cross-correlation between DR7 (top) and DR9 (bottom) quasars and the 100 μm maps. Different coloured symbols correspond to different fields. One DR7 quasar in Boötes lies on top of a bright source which biases our result, indicated by the empty red circles. The filled red circles show the cross-correlation after excluding the aforementioned quasar. The dotted line corresponds to no correlation between quasars and cirrus. The dashed line marks the FWHM of the *IRAS* beam. Data points below the scale of the beam are strongly correlated. Data points from different fields are shifted slightly horizontally for clarity.

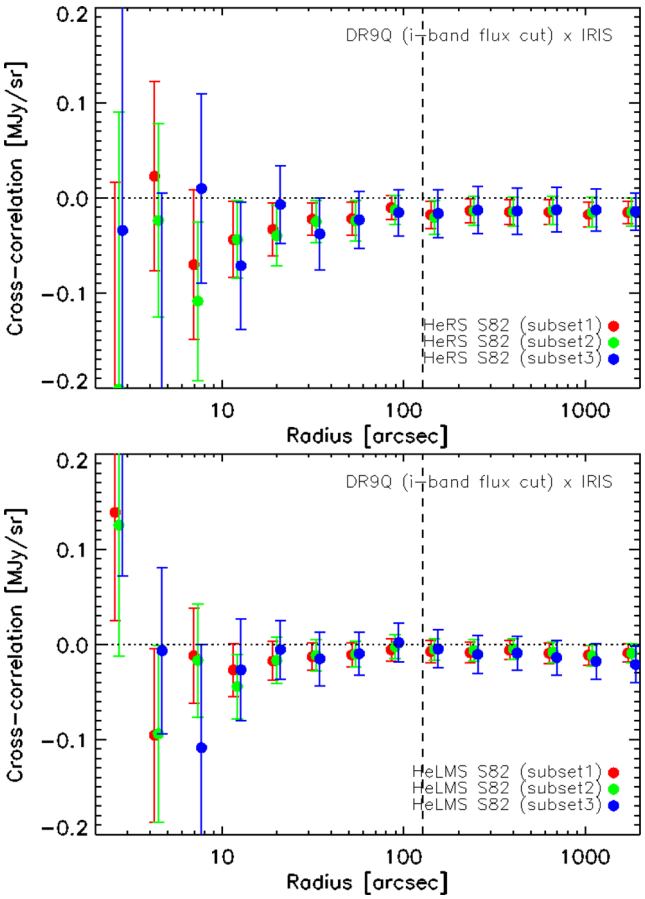

Figure 6. Cross-correlation between DR9 quasars and the 100 μm maps in the HeRS S82 (top) and HeLMS S82 (bottom) region. Different coloured symbols represent quasars with different *i*-band cut (red: $i < 21.2$; green: $i < 21.0$; blue: $i < 20.0$).

3.3 Cross-correlation between quasars and CIB

In the left-hand column of Fig. 8, we plot the cross-correlation between DR7 quasars ($z = [0.15, 2.5]$) and the CIB at 250, 350 and 500 μm in HeRS, HeLMS, Boötes and Lockman-SWIRE. The cross-correlations in different fields are consistent with each other. On small scales, the signal is dominated by the sub-mm emission of the quasars, as indicated by the SPIRE point spread function (PSF) in the corresponding waveband. No fitting is carried out at this stage, so the amplitude of the PSF is only approximate. On larger scales, significant excess signal beyond the PSF is seen in all wavebands in all fields, indicating that there is a population of DSFGs correlated with the quasars. They could be galaxies residing in the same halo as the quasar and galaxies in separate haloes which are correlated with the quasar-hosting halo. In the right-hand column Fig. 8, we plot the cross-correlation between DR9 quasars ($z = [2.2, 3.5]$) and the CIB in HeRS, HeLMS, Boötes and *XMM*-LSS. Again, on small scales, the signal is dominated by the emission of the quasars. On larger scales, excess signal is seen in all fields at all wavelengths. The dispersion in the cross-correlation between different fields is also larger for the DR9 quasars than the DR7 quasars. It could be due to the surface density of the DR9 quasars which is around a factor of 2 lower than that of the DR7 quasars (except in Boötes).

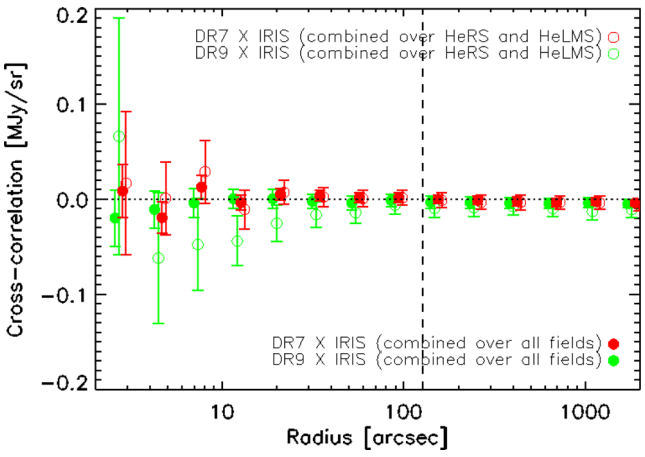

Figure 7. The combined cross-correlation between the quasars (red: DR7; green: DR9) and the 100 μm maps. The filled circles show the combined signal over all fields, while the open circles show the combined results over HeRS and HeLMS.

In Fig. 9, we plot the combined cross-correlation between the quasars and the CIB, using inverse variance weighting. The filled circles are the combined cross-correlation over all fields and the

Downloaded from http://mnras.oxfordjournals.org/ at University of Durham on February 11, 2016

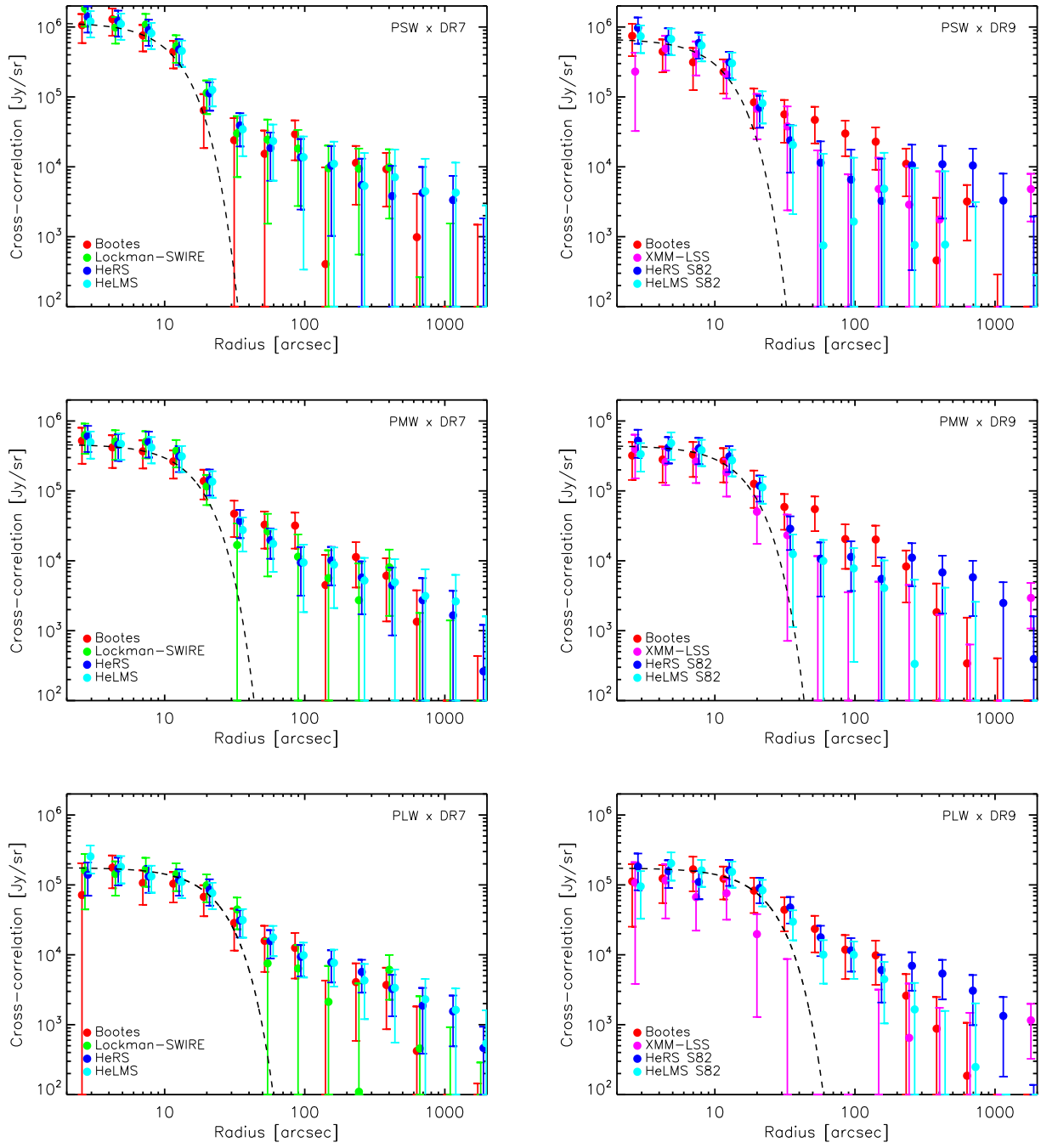

Figure 8. Cross-correlation between quasars (left: DR7; right: DR9) and the CIB at PSW 250 (top), PMW 350 (middle) and PLW 500 (bottom) μm. Different coloured symbols correspond to different fields. Data points from different fields are shifted slightly horizontally. The dashed line illustrates the shape of the SPIRE PSF in the corresponding waveband. The cross-correlation in different fields generally give consistent result. On small scales, the cross-correlation is dominated by the emission of the quasars. On large scales, an excess signal beyond the PSF is seen in almost all cases, due to DSFGs correlated with the quasars.

empty circles are the combined signal using only HeRS and HeLMS. The two different types of combined signal are consistent with each other and exhibit significant excess signal beyond the PSF at all wavelengths. Compared to the DR7 quasars, the emission of the DR9 quasars is slightly weaker in all bands. In Fig. 10, we compare the combined cross-correlation (using all fields) between the quasars and the SPIRE maps at all three wavelengths. For both DR7 and DR9 quasars, the emission of the quasars decreases by almost an order magnitude from 250 to 500 μm, while the change in the correlated emission is much smaller. This is to do with the broadening of the beam from 250 to 500 μm which affects point sources (i.e. the quasars) more than extended structures (i.e. the correlated signal from DSFGs). Another possibility is that the quasars might have a higher dust temperature than the correlated DSFGs.

Downloaded from http://mnras.oxfordjournals.org/ at University of Durham on February 11, 2016

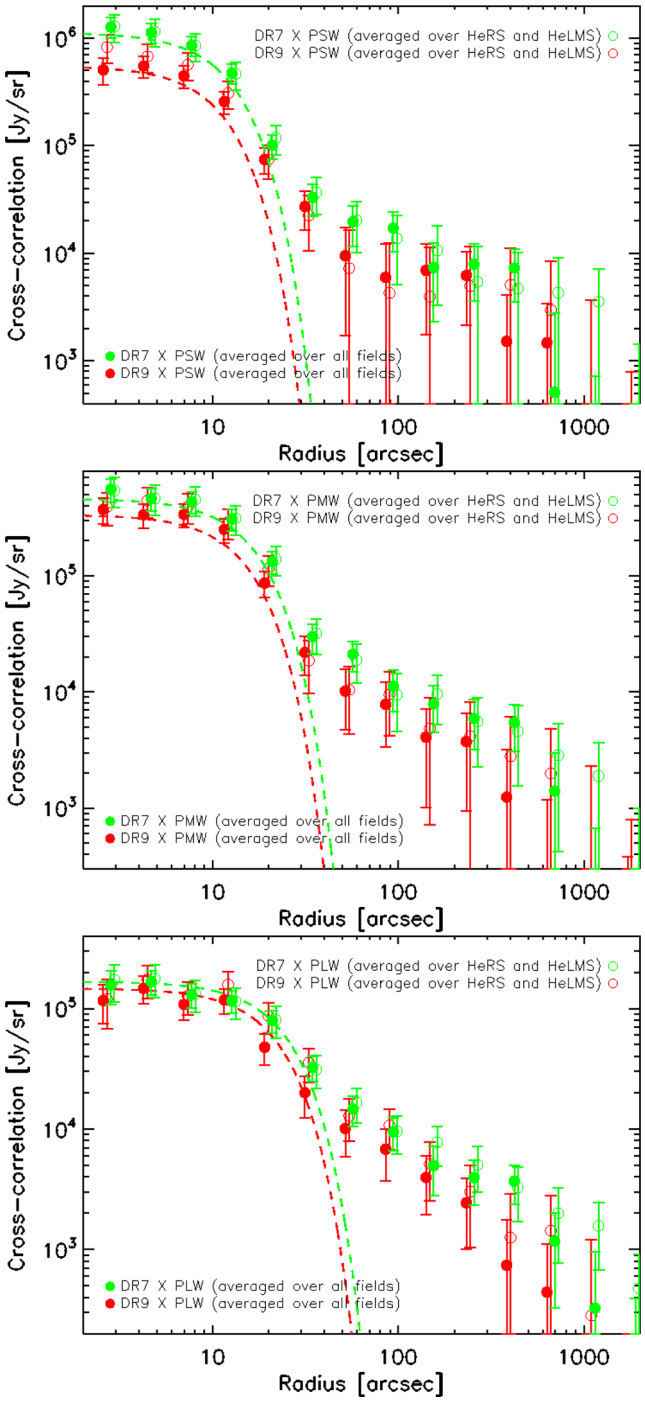

Figure 9. The combined cross-correlation between the quasars (green: DR7; red: DR9) and the CIB (filled circles: combined signal over all fields; empty circles: combined signal over HeRS and HeLMS). The two different types of combined signal agree well with each other. The dashed line illustrates the shape of the PSF in the corresponding waveband.

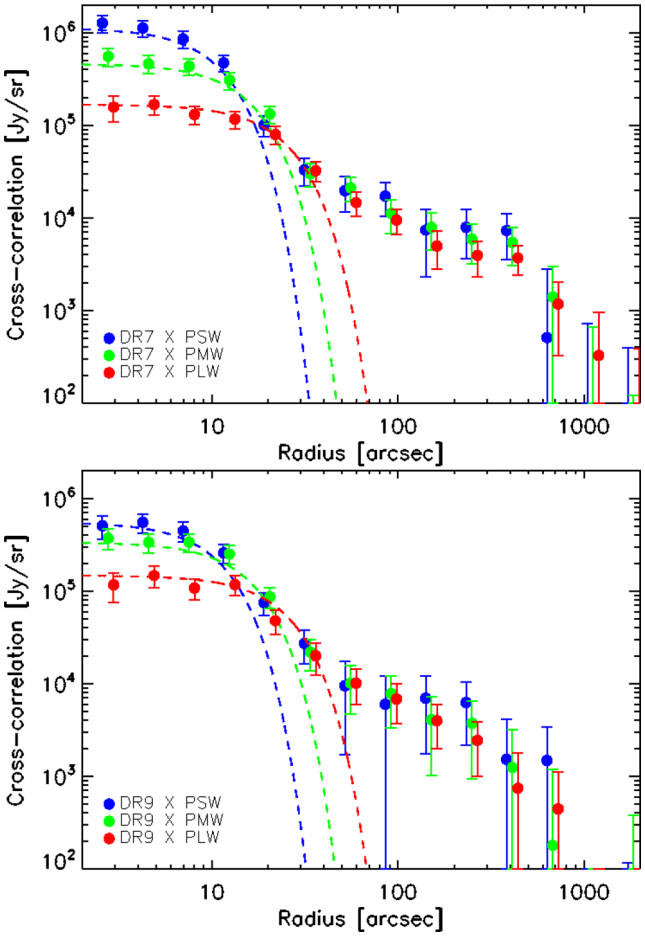

Figure 10. The combined cross-correlation between quasars (top: DR7; bottom: DR9) and the SPIRE maps averaged over all fields. Different coloured symbols correspond to different wavelengths (blue: 250 μm; green: 250 μm; red: 500 μm). The dashed line illustrates the PSF in the corresponding waveband.

4 HALO MODEL OF THE CO-EVOLUTION OF BH GROWTH AND STAR FORMATION

4.1 Halo model of the CIB

The halo model of the CIB anisotropies presented in this paper is identical to the model presented in Viero et al. (2013) and Hajian et al. (in preparation), which is in turned developed based on Shang et al. (2012). For completeness, we outline the main elements of the CIB model here. For more details, please refer to Shang et al. (2012) and Viero et al. (2013) . The power spectra of the CIB sourced by infrared galaxies is composed of a Poisson noise term and a clustered term,

$$P(k_\theta)^{\rm CIB}_{\nu_1\nu 2} = P(k_\theta)^{\rm Poisson}_{\nu_1\nu 2} + P(k_\theta)^{\rm clust}_{\nu_1\nu 2}. \quad (6)$$

The Poisson noise, independent of angular scale, is related to the multidimensional number counts of the infrared sources,

$$P(k_\theta)^{\rm Poisson}_{\nu_1\nu 2} = \int_0^{S_{\rm cut}} S_{\nu_1} S_{\nu_2} \frac{{\rm d}^2 N}{{\rm d}S_{\nu_1}{\rm d}S_{\nu_2}} {\rm d}S_{\nu_1}{\rm d}S_{\nu_2}. \quad (7)$$

The clustered term is the flux averaged projection of the three-dimensional spatial power spectrum,

$$P(k_\theta)^{\rm clust}_{\nu_1\nu_2} = \int \frac{{\rm d}z}{{\rm d}V_{\rm c}/{\rm d}z} P(k, z)^{\rm clust}_{\nu_1\nu_2} \frac{{\rm d}S_{\nu_1}}{{\rm d}z} \frac{{\rm d}S_{\nu_2}}{{\rm d}z}. \quad (8)$$

Here, ${\rm d}V_{\rm c}$ is the comoving volume element, and $\frac{{\rm d}S_\nu}{{\rm d}z}$ is the redshift distribution of the integrated flux at a given frequency which can be calculated as

$$\frac{{\rm d}S_\nu}{{\rm d}z} = \int_0^{S_{\rm cut}} S_\nu \frac{{\rm d}^2 N}{{\rm d}S_\nu {\rm d}z} {\rm d}S_\nu. \quad (9)$$

Downloaded from http://mnras.oxfordjournals.org/ at University of Durham on February 11, 2016

The spatial power spectrum of CIB sources can be decomposed into a one-halo and two-halo term which describes the small-scale clustering due to pairs of galaxies in the same halo and the large-scale clustering due to pairs of galaxies in different haloes, respectively,

$$P(k,z)^{\rm clust}_{\nu_1\nu_2} = P(k,z)^{\rm clust:1h}_{\nu_1\nu_2} + P(k,z)^{\rm clust:2h}_{\nu_1\nu_2}. \quad (10)$$

The non-linear, one-halo term of the CIB clustered term can be calculated as

$$P(k,z)^{\rm clust:1h}_{\nu_1\nu_2} = \frac{1}{\bar{j}_{\nu_1}\bar{j}_{\nu_2}}\int {\rm d}M \frac{{\rm d}N}{{\rm d}M}(z) \times [f^{\rm cen}_{\nu_1}(M,z) f^{\rm sat}_{\nu_2}(M,z) u_{\rm gal}(k,z|M) \quad (11)$$

$$+ f^{\rm cen}_{\nu_2}(M,z) f^{\rm sat}_{\nu_1}(M,z) u_{\rm gal}(k,z|M)$$

$$+ f^{\rm sat}_{\nu_1}(M,z) f^{\rm sat}_{\nu_2}(M,z) u^2_{\rm gal}(k,z|M)]. \quad (12)$$

Here, $f^{\rm cen}_{\nu}(M,z)$ and $f^{\rm sat}_{\nu}(M,z)$ are the luminosity-weighted number of central and satellite galaxies as a function of redshift and halo mass, $\bar{j}_{\nu}(z)$ is the mean comoving specific emission coefficient as a function of redshift, $\frac{{\rm d}N}{{\rm d}M}(z)$ is the redshift-dependent halo mass function (taken from Tinker et al. 2008), $u_{\rm gal}(k,z|M)$ is the normalized Fourier transform of the galaxy density distribution within a halo (assumed to follow the NFW profile in this paper). Here luminosity-weighted number of central and satellite galaxies can be derived as

$$f^{\rm cen}_{\nu}(M,z) = N^{\rm cen}\frac{L^{\rm cen}_{(1+z)\nu}(M,z)}{4\pi} \quad (13)$$

and

$$f^{\rm sat}_{\nu}(M,z) = \int {\rm d}m \frac{{\rm d}n}{{\rm d}m}(M,z)\frac{L^{\rm sat}_{(1+z)\nu}(m,z)}{4\pi}, \quad (14)$$

where m is the sub-halo mass at the time of accretion and $\frac{{\rm d}n}{{\rm d}m}(M,z)$ is the sub-halo mass function (taken from Tinker & Wetzel 2010). Therefore, the mean comoving specific emission coefficient is

$$\bar{j}_{\nu} = \int {\rm d}M \frac{{\rm d}N}{{\rm d}M}(z)[f^{\rm cen}_{\nu}(M,z) + f^{\rm sat}_{\nu}(M,z)]. \quad (15)$$

We assume a lognormal relation between halo mass and infrared luminosity,

$$\Sigma(M) = L_0\, M \frac{1}{\sqrt{2\pi\sigma^2_{\rm L/M}}}\exp\left[-\frac{(\log M - \log M_{\rm peak})^2}{2\sigma^2_{\rm L/M}}\right], \quad (16)$$

where $M_{\rm peak}$ and $\sigma_{\rm L/M}$ is peak halo mass scale and 1σ range of the specific infrared luminosity per unit mass and L_0 is the overall infrared luminosity to halo mass normalization factor. A lower limit on the halo mass $M_{\rm min}$ is applied to the halo mass–infrared luminosity relation. To describe the spectral energy distribution (SED) of the infrared galaxy population, we use a single modified blackbody with two parameters, i.e. dust temperature $T_{\rm dust}$ and emissivity β. In addition, the infrared luminosity is assumed to evolve with redshift as $(1+z)^{\eta}$ over the range $0 < z < 2$ followed by a plateau at $z > 2$. The two-halo term of the CIB clustering power spectrum can be calculated as

$$P(k,z)^{\rm clust:2h}_{\nu_1\nu_2} = \frac{1}{\bar{j}_{\nu_1}\bar{j}_{\nu_2}} P_{\rm lin}(k,z) D(k,z)_{\nu_1} D(k,z)_{\nu_2}, \quad (17)$$

where $P_{\rm lin}(k,z)$ is the linear dark matter power spectrum and

$$D(k,z)_{\nu} = \int {\rm d}M \frac{{\rm d}N}{{\rm d}M} b(M,z) u_{\rm gal}(k,z|M) \times [f^{\rm cen}_{\nu}(M,z) + f^{\rm sat}_{\nu}(M,z)]. \quad (18)$$

Here, $b(M,z)$ is the linear large-scale bias. We use the prescription for the halo bias from Tinker, Wechsler & Zheng (2010) in this paper.

Due to the limited constraining power of the measured cross-correlation between the quasars and the SPIRE maps (quite noisy on large scales), in this paper we use the same parameters of the CIB halo model as in Viero et al. (2013) which fits the auto- and cross-correlation power spectra of the SPIRE maps. The exact values of the parameters used in the CIB model are minimum halo mass $M_{\rm min} = 10^{10.1}\,{\rm M}_{\odot}$, dust temperature $T_{\rm dust} = 24.2$ K, peak halo mass $M_{\rm peak} = 10^{12.1}\,{\rm M}_{\odot}$, $\sigma^2_{\rm L/M} = 0.38$, infrared luminosity to halo mass normalization $L_0 = 10^{-1.71}\,{\rm L}_{\odot}/{\rm M}_{\odot}$, dust emissivity $\beta = 1.45$ and luminosity evolution $\eta = 2.19$.

4.2 Halo model of the quasars

Many studies have used the clustering measurements of quasars to constrain their HODs. Generally, quasars are found to inhabit haloes around a few times $10^{12}\,{\rm M}_{\odot}$ (Porciani, Magliocchetti & Norberg 2004; Croom et al. 2005; Porciani & Norberg 2006; da Ângela et al. 2008; Shen et al. 2009, 2013; Ross et al. 2009; White et al. 2012) . The clustering strength of quasars seems to depend very weakly on quasar luminosity or redshift. It indicates that there is a poor correlation between halo mass and the instantaneous quasar luminosity. Richardson et al. (2012) found tentative evidence for increasing halo mass scale for quasars with increasing redshift. They found that at $z \sim 1.4$ the median halo mass hosting central quasars is around $4.1^{+0.3}_{-0.4} \times 10^{12}\,{\rm M}_{\odot}$ while at $z \sim 3.2$ the median halo mass increases to $14.1^{+5.8}_{-6.9} \times 10^{12}\,{\rm M}_{\odot}$. Most quasars are central galaxies according HOD analysis of quasar clustering statistics. The satellite fraction of quasars is generally found to be of the order a few per cent at most, although the exact satellite fraction estimated from different studies vary significantly from each other. For example, Shen et al. (2013) using a cross-correlation study between the DR7 quasars and DR10 BOSS galaxies estimated the satellite fraction to be $0.068^{+0.034}_{-0.023}$. A similar halo model applied to the auto-correlation of the DR7 quasars combined with a binary quasar sample (Hennawi et al. 2006) in Richardson et al. (2012) inferred the satellite fraction to be $(7.4 \pm 1.3) \times 10^{-4}$.

In this paper, we use a simple halo model for the quasars, widely used in the literature. The quasar mean halo occupation number is composed of central and satellite components,

$$\left\langle N_{\rm q}(M)\right\rangle = \left\langle N^{\rm cen}_{\rm q}(M)\right\rangle + \left\langle N^{\rm sat}_{\rm q}(M)\right\rangle. \quad (19)$$

A softened step function is assumed to describe the central component,

$$N^{\rm cen}_{\rm q}(M) = \frac{1}{2}\left[1 + {\rm erf}\left(\frac{\log{\rm M} - \log{\rm M}_{\rm min}}{\sigma_{\log{\rm M}}}\right)\right] \quad (20)$$

and a rolling-off power law for the satellite component,

$$N^{\rm sat}_{\rm q}(M) = (M/M_1)^{\alpha}\exp(-M_{\rm cut}/M). \quad (21)$$

There are five free parameters in the quasar HOD: $M_{\rm min}$ is the characteristic halo mass scale at which on average half of the dark matter haloes host one quasar as the central galaxy; $\sigma_{\log M}$ is the width of the softened step function; M_1 is the approximate halo mass scale where on average haloes host one satellite quasar; α is the power-law index; $M_{\rm cut}$ is the halo mass scale below which the number of the satellite quasars decreases exponentially.

In principle, we should also multiply a free parameter to the quasar HOD $N_{\rm q}(M)$ to describe the duty cycle of quasars, i.e. only a

Downloaded from http://mnras.oxfordjournals.org/ at University of Durham on February 11, 2016

certain fraction (<1) of the haloes actually host quasars. However, if we assume that quasar duty cycle is independent of halo mass, then it will cancel the duty cycle parameter which will appear in the quasar number density $\bar{n}$ in equations (22) and (23). So, the quasar HOD equations (equations 19– 21) should be interpreted as the number of quasars in haloes of mass M which host quasars (not all haloes of mass M). In addition, we emphasize that while we assume the mean halo occupation number of quasars is independent of redshift, we are not assuming the duty cycle of the quasars is independent of redshift. In the calculation of the 3D spatial cross-correlation between the quasars and the DSFGs comprising the CIB, the duty cycle (assumed to be independent of halo mass) cancels out in the 3D power spectra in each redshift slice before we integrate the 3D spectra to get the angular cross-correlation spectra.

4.3 Halo model of the cross-correlation

Combining the CIB halo model in Section 4.1 and the quasar halo model in Section 4.2, we can model the cross-correlation between the quasars and the CIB. The one-halo term of the cross-correlation power spectrum between quasars and the CIB measured by *Herschel*-SPIRE can be modelled as

$$\begin{aligned} P(k,z)^{\rm 1h}_{\rm sq} = & \frac{1}{j\bar{n}}\int {\rm d}M \frac{{\rm d}N}{{\rm d}M}(z) \\ & \times [f_{\rm s}^{\rm cen}(M,z)N_{\rm q}^{\rm sat}(M,z)u_{\rm gal}(k,z|M) \\ & + f_{\rm s}^{\rm sat}(M,z)N_{\rm q}^{\rm cen}(M,z)u_{\rm gal}(k,z|M) \\ & + f_{\rm s}^{\rm sat}(M,z)N_{\rm q}^{\rm sat}(M,z)u^2_{\rm gal}(k,z|M)]. \end{aligned} \quad (22)$$

The two-halo term of the cross-correlation can be modelled as

$$P(k,z)^{\rm 2h}_{\rm sq} = \frac{1}{j\bar{n}} P_{\rm lin}(k,z) D(k,z)_{\rm s} D(k,z)_{\rm q}, \quad (23)$$

where

$$\begin{aligned} D_{\rm s} = & \int {\rm d}M \frac{{\rm d}N}{{\rm d}M}(z) b(M,z) u_{\rm gal}(k,z|M) \\ & \times [f_{\rm s}^{\rm cen}(M,z) + f_{\rm s}^{\rm sat}(M,z)] \end{aligned} \quad (24)$$

and

$$\begin{aligned} D_{\rm q} = & \int {\rm d}M \frac{{\rm d}N}{{\rm d}M}(z) b(M,z) u_{\rm gal}(k,z|M) \\ & \times [N_{\rm q}^{\rm cen}(M,z) + N_{\rm q}^{\rm sat}(M,z)]. \end{aligned} \quad (25)$$

Under Limber's approximation (Limber 1953), the angular cross-correlation power spectrum between quasars and CIB is related to the spatial power spectrum,

$$P(k_\theta)_{\rm sq} = \int \frac{{\rm d}z}{{\rm d}V_{\rm c}/{\rm d}z} P\,(k,z)_{\rm sq} \frac{{\rm d}S}{{\rm d}z} \frac{{\rm d}N_{\rm q}}{{\rm d}z}, \quad (26)$$

where ${\rm d}V_{\rm c}/{\rm d}z$ is the comoving volume element per unit along the redshift axis, ${\rm d}S/{\rm d}z$ is the redshift distribution of the cumulative CIB flux, and ${\rm d}N_{\rm q}/{\rm d}z$ is the normalized redshift distribution of the quasar sample. The angular correlation function is related to the angular power spectrum

$$w(\theta) = \int \frac{k_\theta {\rm d}k_\theta}{2\pi} P(k_\theta) J_0(k_\theta \theta), \quad (27)$$

where $J_0(x)$ is the zeroth-order Bessel function. Finally, the angular correlation function needs to be convolved with the SPIRE beam, which can be described as a 2D Gaussian. Therefore, the final beam convolved angular cross-correlation between the quasars and the CIB is

$$\begin{aligned} w_{\rm conv}(\theta) = & \frac{1}{2\pi\sigma^2}\int w(|\boldsymbol{\theta}-\boldsymbol{\theta}'|)\exp\left(-\frac{\theta'^2}{2\sigma^2}\right){\rm d}\boldsymbol{\theta}' \\ = & \frac{1}{2\pi\sigma^2}\int_0^{2\pi} w(\sqrt{\theta^2+\theta'^2-2\theta\theta'\cos\phi}){\rm d}\phi \\ & \int \exp\left(-\frac{\theta'^2}{2\sigma^2}\right)\theta'{\rm d}\theta', \end{aligned} \quad (28)$$

where σ is the standard deviation of the Gaussian beam.

4.4 Halo model results

As mentioned earlier, we have used the same parameters of the CIB halo model as in Viero et al. (2013) which fit the auto- and cross-correlation power spectra of the SPIRE maps. In this paper, we only vary the parameters related to the quasars to fit the cross-correlation between the quasars and the CIB. There are eight parameters in our model: five parameters ($M_{\rm min}$, σ_M, α, M_1 and $M_{\rm cut}$) describing the HOD of the quasars; three parameters (A_1, A_2 and A_3) related to the amplitude of the mean infrared emission of the quasars at 250, 350 and 500 μm. We would like to emphasize that the last three parameters (A_1, A_2 and A_3) of the mean infrared emission of the quasars are not part of the halo model of the quasars, i.e. we are not modelling the infrared emission of the quasars in the halo model. The infrared emission of the quasars is directly measured from the cross-correlation signal (equivalent to the stacking signal of the CIB maps at the location of the quasars) on small scales where the emission from the quasars dominate, after subtracting the correlation emission from DSFGs around the quasars.

In Fig. 11, we plot the combined cross-correlation over all fields (black circles) between the quasars and the CIB and the best fit from our model. The dashed line corresponds to the best-fitting mean sub-mm emission of the quasars. The blue solid line corresponds to the best-fitting one-halo term of the cross-correlation convolved with the SPIRE beam, the red solid line corresponds to the best-fitting beam-convolved two-halo term and the black solid line corresponds to the total cross-correlation signal (i.e. the sum of the emission of the quasars and the emission from the correlated DFSGs). With a median redshift $\langle z\rangle$ of 1.4, the mean flux density of the DR7 quasars is $11.1^{+1.6}_{-1.4}$, $7.1^{+1.6}_{-1.3}$ and $3.6^{+1.4}_{-1.0}$ mJy at 250, 350 and 500 μm respectively, while the mean flux density of the DR9 quasars ($\langle z\rangle = 2.5$) is $5.7^{+0.7}_{-0.6}$, $5.0^{+0.7}_{-0.7}$ and $1.8^{+0.5}_{-0.4}$ mJy at 250, 350 and 500 μm respectively. Therefore, the mean sub-mm flux of the quasars in the SPIRE wavebands are generally comparable to the 1σ confusion noise of the maps.

Using a modified blackbody with a dust emissivity of 1.45 combined with the mid-infrared power law ($f_\nu \propto \nu^{-2}$) to describe the SED of the quasars (i.e. the same assumptions we made regarding the SED of the DSFGs in Section 4.1), we can derive the best-fitting dust temperature and total infrared luminosity for the quasars. For the DR7 quasars, the best-fitting dust temperature and infrared luminosity is $39.0^{+11.0}_{-6.3}$ K and $\log_{10} L_{\rm IR}({\rm L}_\odot) = 12.4^{+0.3}_{-0.2}$, respectively. For the DR9 quasars, the best-fitting dust temperature and infrared luminosity is $52.3^{+7.8}_{-5.6}$ K and $\log_{10} L_{\rm IR}({\rm L}_\odot) = 12.8^{+0.1}_{-0.1}$, respectively. The mean infrared luminosity of the quasars seems to indicate that the quasar host galaxies are forming stars at a rate that is comparable to some of the most prodigious star-forming galaxies. Due to the degeneracy between dust temperature and emissivity, the best-fitting temperature decreases with increasing emissivity but

Downloaded from http://mnras.oxfordjournals.org/ at University of Durham on February 11, 2016

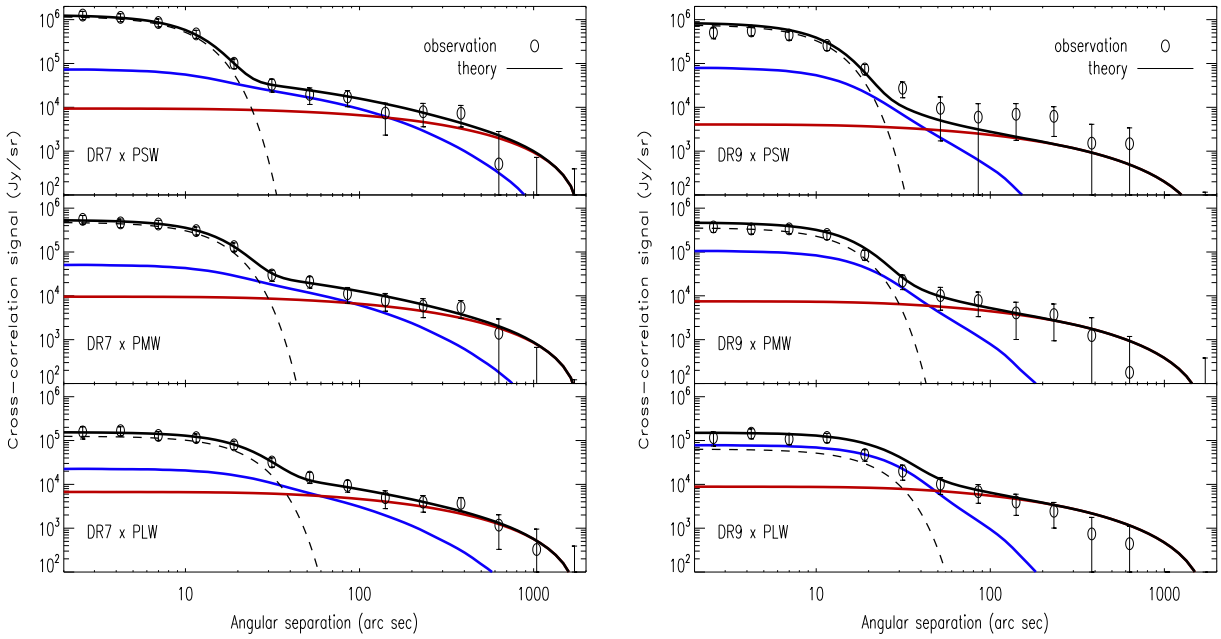

Figure 11. The combined cross-correlation between the quasars (left: DR7; right: DR9) and the CIB (top: 250 μm; middle: 350 μm; bottom: 500 μm) compared with the best fit from the halo model. The dashed line corresponds to the best-fitting mean emission of the quasars. The blue solid line corresponds to the best-fitting one-halo term of the cross-correlation convolved with the SPIRE beam, the red solid line corresponds to the best-fitting two-halo term convolved with the beam. The black circles are the measured cross-correlation. The black solid line is the best-fitting total signal, i.e. the sum of the mean emission of the quasars and the correlated emission from DSFGs.

the best-fitting infrared luminosity is almost unaffected. The higher redshift DR9 quasars are on average brighter than the DR7 quasars, possibly due to elevated star formation activity and/or BH accretion. Another possibility is that for the higher redshift DR9 quasars, we are starting to probe shorter wavelengths where the contribution of the accreting BH to the total infrared luminosity is larger. The dust temperature of the satellite galaxies around DR7 and DR9 quasars is fixed at 24.2 K in the halo model (see Section 4.1) as we use the same CIB halo model parameters as in Viero et al. (2013) which fits the power spectra of the SPIRE maps. As we have used the same SED assumptions for the quasars and the DSFGs, we can directly compare the estimated temperatures for both populations. Both DR7 and DR9 quasars are hotter than the correlated DSFGs.

In Fig. 12, we plot the mean HOD of the DR7 and DR9 quasars, decomposed into central and satellite components. The shaded region indicates the 68 per cent confidence intervals. The red, blue and green solid lines represent the best-fitting value for $M_{\rm min}$ (the characteristic halo mass scale at which on average half of the haloes host one central quasar), $M_{\rm cut}$ (the halo mass scale below which the HOD for the satellite quasars decays exponentially) and M_1 (the halo mass for hosting on average one satellite quasar), respectively. For the DR7 quasars, the host halo mass scale for the central and satellite quasars is $M_{\rm min} = 10^{12.4\pm0.9}$ M$_\odot$ and $M_1 = 10^{13.6\pm0.4}$ M$_\odot$, respectively. For the DR9 quasars, the host halo mass scale for the central and satellite quasars is $M_{\rm min} = 10^{12.3\pm0.6}$ M$_\odot$ and $M_1 = 10^{12.8\pm0.4}$ M$_\odot$, respectively. The typical halo environment of the DR7 and DR9 quasars we find in this study is similar to previous studies using quasar auto-correlation statistics (e.g. Shen et al. 2009; White et al. 2012; Richardson et al. 2012), as expected. Tables 2 and 3 list the best-fitting values, uncertainties and correlations of the parameters in the halo model for the DR7 and DR9 quasars. From the HODs, we find that the satellite fraction (the ratio of satellite quasars to the total number of quasars) is $0.008^{+0.008}_{-0.005}$ and $0.065^{+0.021}_{-0.031}$ for the DR7 and DR9 quasars, respectively. Our estimate of the satellite fraction must be taken with great caution as the satellite fraction is known to be very sensitive to the specific parameterisations of the quasar HOD. None the less, our estimates are broadly consistent with other studies, i.e. the quasar satellite fraction is found to be around a few per cent at most. Thus, the majority of the DR7 and DR9 quasars are expected to be central galaxies and the correlated DSFGs in the one-halo term are mostly satellites in the same halo.

5 DISCUSSIONS AND CONCLUSIONS

We present the first cross-correlation measurement between optically selected type 1 SDSS DR7 and DR9 quasars and the CIB measured by *Herschel*-SPIRE at 250, 350 and 500 μm. The distribution of the quasars at $0.15 < z < 3.5$ (DR7: $0.15 < z < 2.5$; DR9: $2.2 < z < 3.5$) covers the redshift range where we expect most of the CIB to originate. We detect the sub-mm emission of the quasars which dominates on small scales as well as the correlated emission from DSFGs dominant on larger scales.

A halo model is used to interpret the measured cross-correlation between the quasars and the CIB. At a median redshift of 1.4, the mean flux density of the DR7 quasars is $11.1^{+1.6}_{-1.4}$, $7.1^{+1.6}_{-1.3}$ and $3.6^{+1.4}_{-1.0}$ mJy at 250, 350 and 500 μm, respectively. At a median redshift of 2.5, the mean flux density of the DR9 quasars is $5.7^{+0.7}_{-0.6}$, $5.0^{+0.8}_{-0.7}$ and $1.8^{+0.5}_{-0.4}$ mJy at 250, 350 and 500 μm, respectively. By fitting a modified blackbody SED combined with a mid-infrared power-law template to the mean sub-mm fluxes, we find that the higher redshift DR9 quasars have a higher mean infrared luminosity ($\log_{10}L_{\rm IR}(\rm L_\odot) = 12.8$) than the DR7 quasars ($\log_{10}L_{\rm IR}(\rm L_\odot) = 12.4$), possibly due to elevated star formation activity and/or BH accretion or a larger contribution to the infrared luminosity from the accreting BH. Further investigation of the power source of the

Downloaded from http://mnras.oxfordjournals.org/ at University of Durham on February 11, 2016

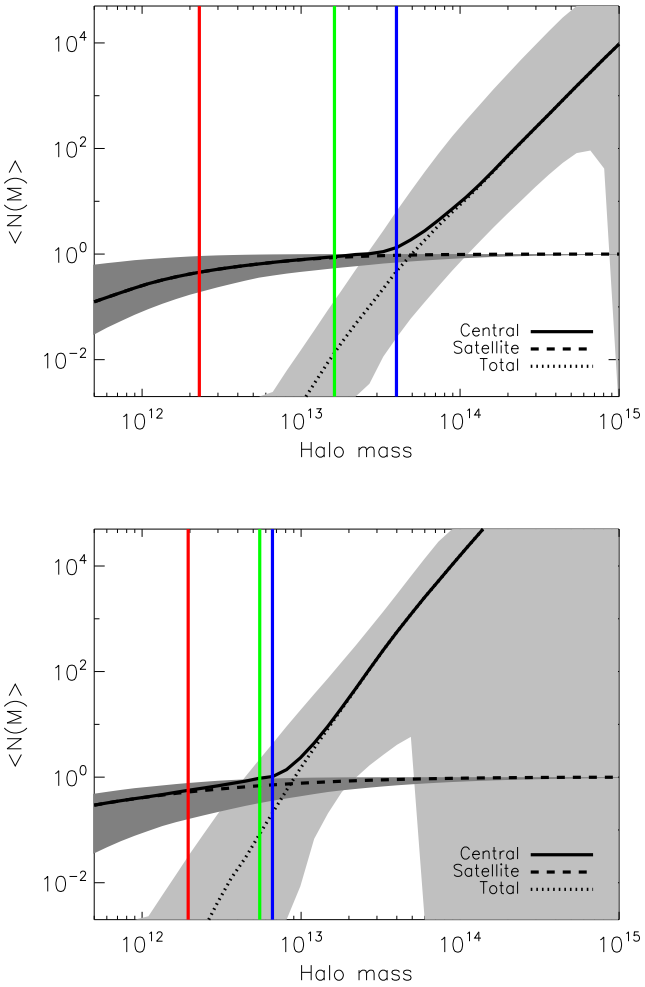

Figure 12. The mean HOD of quasars (top: DR7; bottom: DR9), decomposed into central and satellite components. The shaded region indicate the 68 per cent confidence intervals. The red, green and blue solid line represents the best fit $M_{\rm min}$ (the characteristic halo mass scale at which on average half of the haloes host one central quasar), $M_{\rm cut}$ (the halo mass scale below which the HOD for the satellite quasars decays exponentially) and M_1 (the halo mass scale for hosting on average one satellite quasar), respectively. The quasar HODs should be interpreted as the number of quasars in haloes of mass M which host quasars, not all haloes of mass M (see discussions in Section 4.2).

infrared luminosity of the quasars is beyond the scope of this paper. We find that the correlated sub-mm emission arises from satellite DSFGs in the same halo as the central quasar (the one-halo term) and DSFGs in separate haloes correlated with the quasar-hosting halo (the two-halo term).

We infer from the halo model that the satellite fraction of the DR7 quasars (z = [0.15, 2.5]) at a median redshift $\langle z \rangle$ of 1.4 is $0.008^{+0.008}_{-0.005}$, and the host halo mass scale for the central and satellite quasars is $M_{\rm min} = 10^{12.4 \pm 0.9}$ M$_\odot$ and $M_1 = 10^{13.6 \pm 0.4}$ M$_\odot$, respectively. The satellite fraction of the DR9 quasars (z = [2.2, 3.5]) at a median redshift $\langle z \rangle$ of 2.5 is $0.065^{+0.021}_{-0.031}$, and the host halo mass scale for the central and satellite quasars is $M_{\rm min} = 10^{12.3 \pm 0.6}$ M$_\odot$ and $M_1 = 10^{12.8 \pm 0.4}$ M$_\odot$, respectively. Therefore, the typical halo environment of the quasars is similar to that of the most actively star-forming DSFGs over the redshift range probed. This is expected if dusty starburst and quasar activity are evolutionarily linked phenomena.

Many aspects of our study can be improved and/or extended. In this paper, we have used the cross-correlation signal between the quasar samples and the CIB maps to constrain the halo occupation statistics of the quasars, leaving the CIB halo model fixed. A more complete approach would be to combine the auto-correlation statistics (of the quasars and the CIB maps separately) and the cross-correlation statistics (between the two tracers) to constrain the connection between different types of galaxies and the underlying dark matter haloes simultaneously, varying parameters in both the quasar halo model and the CIB halo model at the same time. We leave this project to a future paper when we have a better understanding of the quasar selection effects in the Stripe 82 region. In the halo model of the quasar population, we have assumed that the duty cycle of the quasars is independent of halo mass and redshift, and the duty cycle is the same for central and satellite quasars. In principle, one could explore using mass-dependent and time-dependent duty cycles for the quasars as well as different duty cycles for the central and satellite quasars (Shen et al. 2010).

In the quasar halo model and the CIB halo model, we have not considered scatter in the quasar number–halo mass relation or scatter in the infrared luminosity–halo mass relation. Exploring the consequences of different variations in the halo model of the quasars or the CIB from the simple models assumed in this paper is well beyond the scope of this work. Many empirical studies and theoretical studies have suggested that the dominant quasar trigger mechanism may change from mergers to secular processes (e.g. Vittorini, Shankar & Cavaliere 2005; Hopkins & Hernquist 2009; Draper & Ballantyne 2012). In the next few years, the number of optically selected quasars is expected to rise sharply thanks to surveys such as eBOSS and DESI. So, we can expect the signal to noise of the clustering measurement will be much improved when we divide quasars into finer redshift bins. We defer a thorough investigation of different HOD parametrizations and the evolution of various HOD parameters with cosmic time to future papers.

ACKNOWLEDGEMENTS

LW and PN acknowledge support from an ERC StG grant (DEGAS-259586).

SPIRE has been developed by a consortium of institutes led by Cardiff Univ. (UK) and including Univ. Lethbridge (Canada); NAOC (China); CEA, LAM (France); IFSI, Univ. Padua (Italy); IAC (Spain); Stockholm Observatory (Sweden); Imperial College London, RAL, UCL-MSSL, UKATC, Univ. Sussex (UK); Caltech, JPL, NHSC, Univ. Colorado (USA). This development has been supported by national funding agencies: CSA (Canada); NAOC (China); CEA, CNES, CNRS (France); ASI (Italy); MCINN (Spain); SNSB (Sweden); STFC (UK); and NASA (USA).

Funding for the SDSS and SDSS-II has been provided by the Alfred P. Sloan Foundation, the Participating Institutions, the National Science Foundation, the US Department of Energy, the National Aeronautics and Space Administration, the Japanese Monbukagakusho, the Max Planck Society, and the Higher Education Funding Council for England. The SDSS website is http://www.sdss.org/.

The SDSS is managed by the Astrophysical Research Consortium for the Participating Institutions. The Participating Institutions are the American Museum of Natural History, Astrophysical Institute Potsdam, University of Basel, University of Cambridge, Case Western Reserve University, University of Chicago, Drexel University, Fermilab, the Institute for Advanced Study, the Japan Participation Group, Johns Hopkins University, the Joint

Downloaded from http://mnras.oxfordjournals.org/ at University of Durham on February 11, 2016

Table 2. Best-fitting values, uncertainties and correlations of the model parameters for the DR7 quasars. The first five parameters ($M_{\rm min}$, σ_M, α, M_1 and $M_{\rm cut}$) describe the HODs of the DR7 quasars while the last three parameters (A_1, A_2 and A_3) correspond to the mean flux (in unit of Jy sr^{-1}) of the DR7 quasars at 250, 350 and 500 μm, respectively. Using the SPIRE beam area (0.9942, 1.765, and 3.730 × 10^{-8} sr at 250, 350, and 500 μm, respectively), we can convert the mean flux of the DR7 quasars into $11.1^{+1.6}_{-1.4}$, $7.1^{+1.6}_{-1.3}$ and $3.6^{+1.4}_{-1.0}$ mJy at 250, 350 and 500 μm, respectively.

Parameter	$\log_{10}M_{\rm min}$	σ_M	α	$\log_{10}M_1$	$\log_{10}M_{\rm cut}$	$\log_{10}A_1$	$\log_{10}A_2$	$\log_{10}A_3$
$\log_{10}M_{\rm min}$	12.4 ± 0.9	0.13	−0.08	0.72	−0.10	−0.41	−0.44	−0.45
σ_M	–	1.1 ± 0.5	0.32	−0.27	0.20	0.36	0.43	0.47
α	–	–	3.0 ± 0.5	0.19	-0.10	0.21	0.29	0.30
$\log_{10}M_1$	–	–	–	13.6 ± 0.4	−0.44	-0.61	−0.65	-0.69
$\log_{10}M_{\rm cut}$	–	–	–	–	13.2 ± 0.5	0.29	0.36	0.39
$\log_{10}A_1$	–	–	–	–	–	6.1 ± 0.1	0.62	0.69
$\log_{10}A_2$	–	–	–	–	–	–	5.6 ± 0.1	0.79
$\log_{10}A_3$	–	–	–	–	–	–	–	5.0 ± 0.14

Table 3. Similar to Table 2 but for DR9 quasars. Using the SPIRE beam area, we can convert the mean flux of the DR9 quasars into $5.7^{+0.7}_{-0.6}$, $5.0^{+0.8}_{-0.7}$ and $1.8^{+0.5}_{-0.4}$ mJy at 250, 350 and 500 μm, respectively.

Parameter	$\log_{10}M_{\rm min}$	σ_M	α	$\log_{10}M_1$	$\log_{10}M_{\rm cut}$	$\log_{10}A_1$	$\log_{10}A_2$	$\log_{10}A_3$
$\log_{10}M_{\rm min}$	12.3 ± 0.6	0.24	−0.38	0.52	−0.30	−0.02	−0.08	−0.10
σ_M	–	1.3 ± 0.5	0.20	−0.49	−0.21	−0.05	−0.18	−0.26
α	–	–	3.21 ± 0.6	−0.2	0.19	0.06	0.04	0.05
$\log_{10}M_1$	–	–	–	12.8 ± 0.4	−0.25	0.10	0.10	0.19
$\log_{10}M_{\rm cut}$	–	–	–	–	12.7 ± 0.6	0.13	0.29	0.35
$\log_{10}A_1$	–	–	–	–	–	5.8 ± 0.1	0.21	0.20
$\log_{10}A_2$	–	–	–	–	–	–	5.5 ± 0.1	0.49
$\log_{10}A_3$	–	–	–	–	–	–	–	4.7 ± 0.1

Institute for Nuclear Astrophysics, the Kavli Institute for Particle Astrophysics and Cosmology, the Korean Scientist Group, the Chinese Academy of Sciences (LAMOST), Los Alamos National Laboratory, the Max-Planck-Institute for Astronomy (MPIA), the Max-Planck-Institute for Astrophysics (MPA), New Mexico State University, Ohio State University, University of Pittsburgh, University of Portsmouth, Princeton University, the United States Naval Observatory and the University of Washington.

Funding for SDSS-III has been provided by the Alfred P. Sloan Foundation, the Participating Institutions, the National Science Foundation and the US Department of Energy Office of Science. The SDSS-III website is http://www.sdss3.org/.

SDSS-III is managed by the Astrophysical Research Consortium for the Participating Institutions of the SDSS-III Collaboration including the University of Arizona, the Brazilian Participation Group, Brookhaven National Laboratory, Carnegie Mellon University, University of Florida, the French Participation Group, the German Participation Group, Harvard University, the Instituto de Astrofisica de Canarias, the Michigan State/Notre Dame/JINA Participation Group, Johns Hopkins University, Lawrence Berkeley National Laboratory, Max Planck Institute for Astrophysics, Max Planck Institute for Extraterrestrial Physics, New Mexico State University, New York University, Ohio State University, Pennsylvania State University, University of Portsmouth, Princeton University, the Spanish Participation Group, University of Tokyo, University of Utah, Vanderbilt University, University of Virginia, University of Washington and Yale University.

REFERENCES

Abazajian K. N. et al., 2009, ApJS, 182, 543
Ahn C. P. et al., 2012, ApJS, 203, 21
Béthermin M., Dole H., Lagache G., Le Borgne D., Penin A., 2011, A&A, 529, A4
Béthermin M. et al., 2012, ApJ, 757, L23
Bonfield D. G. et al., 2011, MNRAS, 416, 13
Bovy J., Hogg D. W., Roweis S. T., 2009, ApJ, 700, 1794
Bovy J. et al., 2011, ApJ, 729, 141
Boyle B. J., Terlevich R. J., 1998, MNRAS, 293, L49
Busca N. G. et al., 2013, A&A, 552, A96
Clements D. L. et al., 2009, ApJ, 698, L188
Croom S. M. et al., 2005, MNRAS, 356, 415
da Ângela J. et al., 2008, MNRAS, 383, 565
Dai Y. S. et al., 2012, ApJ, 753, 33
Dawson K. S. et al., 2013, AJ, 145, 10
Delubac T. et al., 2015, A&A, 574, A59
Dole H. et al., 2006, A&A, 451, 417
Draper A. R., Ballantyne D. R., 2012, ApJ, 751, 72
Eisenstein D. J. et al., 2011, AJ, 142, 72
Fabian A. C., 2012, ARA&A, 50, 455
Fan X., 1999, AJ, 117, 2528
Ferrarese L., Merritt D., 2000, ApJ, 539, L9
Fixsen D. J., Dwek E., Mather J. C., Bennett C. L., Shafer R. A., 1998, ApJ, 508, 123
Franceschini A., Hasinger G., Miyaji T., Malquori D., 1999, MNRAS, 310, L5
Gebhardt K. et al., 2000, ApJ, 539, L13
Giannantonio T., Crittenden R., Nichol R., Ross A. J., 2012, MNRAS, 426, 2581
Griffin M. J. et al., 2010, A&A, 518, L3
Hennawi J. F. et al., 2006, AJ, 131, 1
Hopkins P. F., Hernquist L., 2009, ApJ, 698, 1550
Kayo I., Oguri M., 2012, MNRAS, 424, 1363
Kormendy J., Ho L. C., 2013, ARA&A, 51, 511
Kormendy J., Richstone D., 1995, ARA&A, 33, 581
Kormendy J., Bender R., Cornell M. E., 2011, Nature, 469, 374
Lagache G., Puget J.-L., Gispert R., 1999, Ap&SS, 269, 263
Landy S. D., Szalay A. S., 1993, ApJ, 412, 64

Downloaded from http://mnras.oxfordjournals.org/ at University of Durham on February 11, 2016

Levenson L. et al., 2010, MNRAS, 409, 83
Limber D. N., 1953, ApJ, 117, 134
Lutz D. et al., 2008, ApJ, 684, 853
Magorrian J. et al., 1998, AJ, 115, 2285
Marsden G. et al., 2009, ApJ, 707, 1729
Merloni A., Rudnick G., Di Matteo T., 2004, MNRAS, 354, L37
Miville-Deschênes M.-A., Lagache G., 2005, ApJS, 157, 302
Miville-Deschênes M.-A., Lagache G., Puget J.-L., 2002, A&A, 393, 749
Neugebauer G. et al., 1984, ApJ, 278, L1
Norberg P., Baugh C. M., Gaztañaga E., Croton D. J., 2009, MNRAS, 396, 19
Oliver S. J. et al., 2012, MNRAS, 424, 1614
Padmanabhan N., Hirata C. M., Seljak U., Schlegel D. J., Brinkmann J., Schneider D. P., 2005, Phys. Rev. D, 72, 043525
Palanque-Delabrouille N. et al., 2011, A&A, 530, A122
Palanque-Delabrouille N. et al., 2013, A&A, 551, A29
Pâris I. et al., 2012, A&A, 548, A66
Pénin A. et al., 2012, A&A, 543, A123
Pietrobon D., Balbi A., Marinucci D., 2006, Phys. Rev. D, 74, 043524
Pilbratt G. L. et al., 2010, A&A, 518, L1
Porciani C., Norberg P., 2006, MNRAS, 371, 1824
Porciani C., Magliocchetti M., Norberg P., 2004, MNRAS, 355, 1010
Puget J.-L., Abergel A., Bernard J.-P., Boulanger F., Burton W. B., Desert F.-X., Hartmann D., 1996, A&A, 308, L5
Richards G. T. et al., 2002, AJ, 123, 2945
Richards G. T. et al., 2006, AJ, 131, 2766
Richardson J., Zheng Z., Chatterjee S., Nagai D., Shen Y., 2012, ApJ, 755, 30
Ross N. P. et al., 2009, ApJ, 697, 1634
Ross N. P. et al., 2012, ApJS, 199, 3
Ross N. P. et al., 2013, ApJ, 773, 14
Schlegel D. J., Finkbeiner D. P., Davis M., 1998, ApJ, 500, 525
Schneider D. P. et al., 2010, AJ, 139, 2360
Serjeant S. et al., 2010, A&A, 518, L7
Shang C., Haiman Z., Knox L., Oh S. P., 2012, MNRAS, 421, 2832
Shankar F., Mathur S., 2007, ApJ, 660, 1051
Shen Y. et al., 2009, ApJ, 697, 1656
Shen Y. et al., 2010, ApJ, 719, 1693
Shen Y. et al., 2011, ApJS, 194, 45
Shen Y. et al., 2013, ApJ, 778, 98
Shi Y., Rieke G. H., Ogle P., Jiang L., Diamond-Stanic A. M., 2009, ApJ, 703, 1107
Silverman J. D. et al., 2008, ApJ, 679, 118
Slosar A. et al., 2013, J. Cosmol. Astropart. Phys., 4, 026
Swanson M. E. C., Tegmark M., Hamilton A. J. S., Hill J. C., 2008, MNRAS, 387, 1391
Swinyard B. M. et al., 2010, A&A, 518, L4
Tinker J. L., Wetzel A. R., 2010, ApJ, 719, 88
Tinker J., Kravtsov A. V., Klypin A., Abazajian K., Warren M., Yepes G., Gottlöber S., Holz D. E., 2008, ApJ, 688, 709
Tinker J. L., Wechsler R. H., Zheng Z., 2010, ApJ, 709, 67
Tremaine S. et al., 2002, ApJ, 574, 740
Valiante E., Lutz D., Sturm E., Genzel R., Chapin E. L., 2009, ApJ, 701, 1814
Viero M. P. et al., 2013, ApJ, 772, 77
Viero M. P. et al., 2014, ApJS, 210, 22
Vittorini V., Shankar F., Cavaliere A., 2005, MNRAS, 363, 1376
Wall J. V., Pope A., Scott D., 2008, MNRAS, 383, 435
White M. et al., 2012, MNRAS, 424, 933
York D. G. et al., 2000, AJ, 120, 1579

APPENDIX A: IRIS 100 μm MAPS

The IRIS 100 μm maps in HeRS and HeLMS are plotted in Fig. A1. The IRIS 100 μm maps in Boötes, Lockman-SWIRE and *XMM*-LSS are plotted in Fig. A2. Visually, extended diffuse Galactic cirrus emission are the dominant structures in these maps, especially in HeRS and HeLMS. We estimate that the fractional contribution of the CIB to the 100 μm maps in HeLMS, HeRS, *XMM*-LSS, Boötes and Lockman-SWIRE is 16, 17, 21, 34 and 44 per cent, respectively.

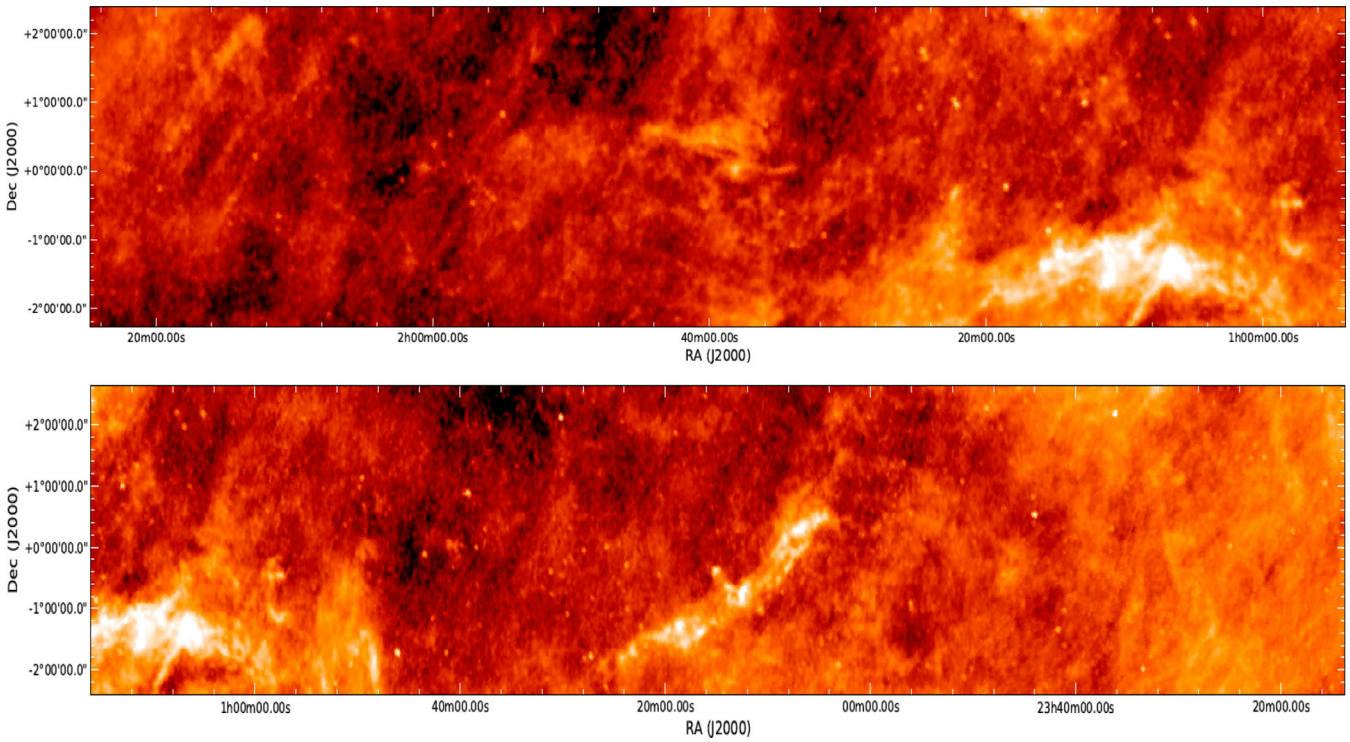

Figure A1. The IRIS 100 μm maps in the HeRS (top) and HeLMS (bottom) field. The dominant signal in these maps comes from extended diffuse Galactic dust emission.

Downloaded from http://mnras.oxfordjournals.org/ at University of Durham on February 11, 2016

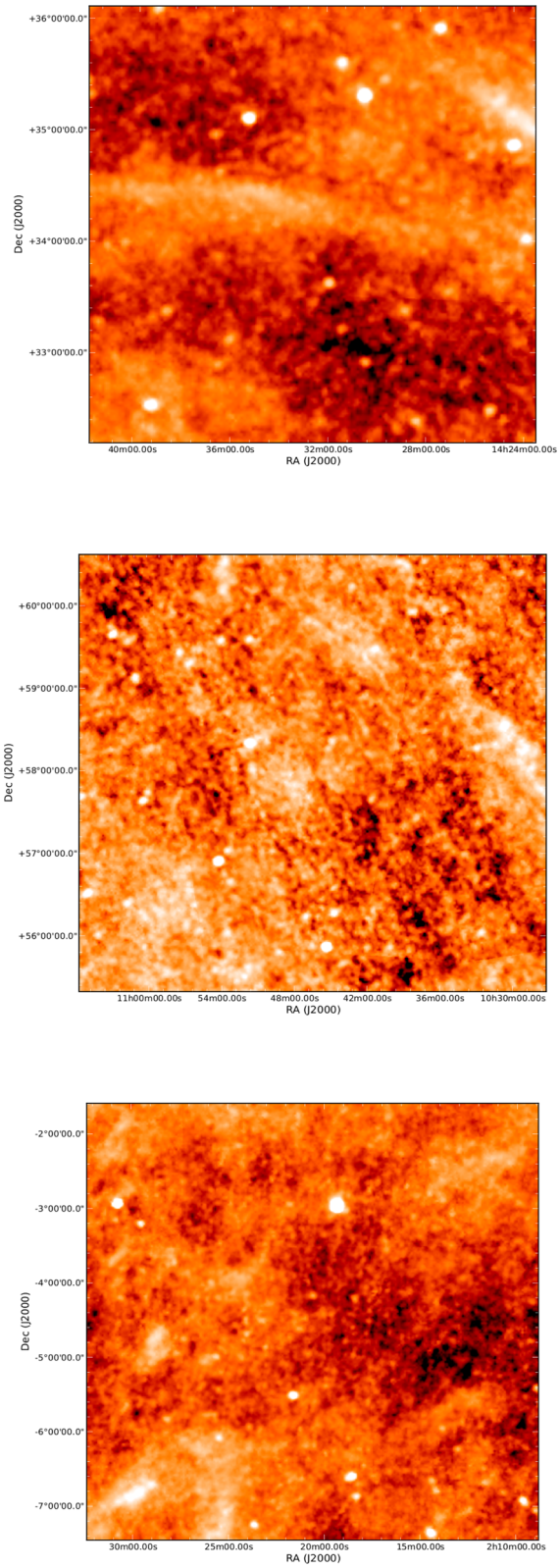

Figure A2. The IRIS 100 μm maps in the Boötes (top), Lockman-SWIRE (middle) and *XMM*-LSS (bottom) field.

APPENDIX B: STACKING

We have a quasar catalogue from which build the quasar density map Q, which gives the number of quasars in each pixel of the map. The mean value of this map is $\bar{Q} = N_{\rm obj}/N_{\rm pix}$, where $N_{\rm obj}$ is the number of objects in the catalogue and $N_{\rm pix}$ is the number of pixels in the map. The SPIRE map M has a mean value $\bar{M}$ which is set to zero, as SPIRE has no sensitivity to the absolute zero-level on the sky. We retain the mean value in what follows to keep the equations general.

The covariance of Q and M is defined as

$$\begin{aligned}\mathrm{Cov}(Q, M) &= \langle (Q - \bar{Q})(M - \bar{M}) \rangle \\ &= \frac{1}{N_{\rm pix}} \sum_{i'=1}^{N_x} \sum_{j'=1}^{N_y} (Q_{i'j'} - \bar{Q})(M_{i'j'} - \bar{M}), \end{aligned} \tag{B1}$$

where the sums are over the two map dimensions and $N_{\rm pix} = N_x N_y$. As shown in Marsden et al. (2009), this is equivalent to what is often called a 'stack', when normalized by $\bar{Q}$, the average number of quasars per pixel:

$$S = \frac{1}{\bar{Q}} \mathrm{Cov}(Q, M). \tag{B2}$$

We can extend equation (B1) to describe a stacked thumbnail, made by making a pixel-by-pixel average of map cutouts centred on each source. This is equivalent to calculating the covariance of two maps with a relative shift by i, j pixels:

$$\begin{aligned}\mathrm{Cov}_{ij}(Q, M) = &\frac{1}{(N_x - i)(N_y - j)} \sum_{i'} \sum_{j'} \\ &(Q_{i'j'} - \bar{Q})(M_{(i'+i)(j'+j)} - \bar{M}). \end{aligned} \tag{B3}$$

In order to account for the edges of the maps, the sum over $i'(j')$ runs from the larger of 1 and i (j) to the smaller of N_x (N_y) and $N_x - i$ ($N_y - j$). $\mathrm{Cov}_{ij}(Q, M)$ is thus a map with indices running from $-N_{\rm thumb}/2$ to $N_{\rm thumb}/2$ for an $N_{\rm thumb} \times N_{\rm thumb}$ thumbnail map. We can then take an azimuthal average of this map to create the radial profile of the stack:

$$R_k(Q, M) = \frac{1}{N_k} \sum_{i,j \in \xi_k} \mathrm{Cov}_{ij}(Q, M), \tag{B4}$$

where ξ_k is the set of pixels for which:

$$k \leq \sqrt{i^2 + j^2} < k + 1, \tag{B5}$$

and N_k is the number of pixels in ξ_k. Using equation (B2), the radial stack S_θ is then

$$S_\theta = \frac{1}{\bar{Q}} R_k(Q, M). \tag{B6}$$

In Section 3.1, we use a modification of the Landy & Szalay (1993) two-point correlation function estimator,

$$w(\theta) = \frac{D_1 D_2(\theta) - D_1 R_1(\theta) - R_1 D_1(\theta) + R_1 R_2(\theta)}{R_1 R_2(\theta)}. \tag{B7}$$

Here, D_1 and D_2 represent the quasar density map and SPIRE map, called Q and M above. R_1 and R_2 represent random realisations of these two data sets. The quantities $X_1X_2(\theta)$ are the same as $R_k(X_1, X_2)$ in equation (B4) above, although without the subtractions of the map means in equation (B3); for convenience, we refer to the non-mean-subtracted version of equation (B4) as $\tilde{R}_k(X_1, X_2)$. The first term in equation (B7) can then be precisely defined as $\tilde{R}_k(Q, M)$. The remaining terms all involve one or more random distributions, and thus in each term, the two quantities are uncorrelated. For

Downloaded from http://mnras.oxfordjournals.org/ at University of Durham on February 11, 2016

uncorrelated distributions, the expectation value of the product of the two variables is equal to the product of the expectation values of each variable, $\langle xy \rangle = \langle x \rangle \langle y \rangle$, and so the remaining terms are simply to the product of the mean values, $\bar{Q}\bar{M}$. We can thus simplify equation (B7):

$$w(\theta) = \frac{\tilde{R}_k(Q, M) - \bar{Q}\bar{M}}{\bar{Q}\bar{M}}. \quad \text{(B8)}$$

By expanding equation (B3), equation (B6) can similarly be rewritten in terms of $\tilde{R}_k$:

$$S_\theta = \frac{1}{\bar{Q}}[\tilde{R}_k(Q, M) - \bar{Q}\bar{M}]. \quad \text{(B9)}$$

The denominator of equation (B7) is zero when the SPIRE map mean is zero, and so we modify the equation by multiplying both sides by the mean $\bar{M}$. We see that the algorithm used in Section 3.1 is thus exactly equivalent to equation (B6), the azimuthally-averaged stacked thumbnail image.

This paper has been typeset from a TEX/LATEX file prepared by the author.

Downloaded from http://mnras.oxfordjournals.org/ at University of Durham on February 11, 2016